

# Loading non-Maxwellian Velocity Distributions in Particle Simulations

Seiji Zenitani

*Space Research Institute, Austrian Academy of Sciences, 8042 Graz, Austria*<sup>\*</sup>

Shunsuke Usami

*National Institute for Fusion Science, Toki 509-5292, Japan*

Shuichi Matsukiyo

*Faculty of Engineering Sciences, Kyushu University 6-1 Kasuga-Koen, Kasuga, Fukuoka 816-8580, Japan*

Numerical procedures for generating non-Maxwellian velocity distributions in particle simulations are presented. First, Monte Carlo methods for an  $(r, q)$  distribution that generalizes flattop and Kappa distributions are discussed. Then, two rejection methods for the regularized Kappa distribution are presented, followed by a comparison in the  $\kappa$  space. A simple recipe is proposed for the subtracted Kappa distribution. Properties and numerical recipes for the ring and shell distributions with a finite Gaussian width are discussed. The ring and shell Maxwellians are further introduced as alternatives to the ring and shell distributions. Finally, methods for the super-Gaussian and the filled-shell distributions are presented.

## I. INTRODUCTION

Plasma velocity distribution functions (VDFs) show many different shapes in the heliosphere. Since the mean free path is much longer than the typical length scale, local VDFs deviate significantly from a Maxwell distribution. In the presence of a planetary dipole field, the VDF is often loss-cone-shaped, because particles with field-aligned velocities escape to the planet. The loss-cone VDF leads to pressure anisotropy, which in turn generates various plasma waves in planetary magnetospheres. VDFs sometimes exhibit a power-law tail in the high-energy part. Such VDFs are often approximated by a generalized Lorentzian distribution, now widely known as the Kappa distribution [31, 46]. The Kappa distribution has drawn significant attention in plasma physics, because it might be an outcome of long-range interaction between charged particles [20, 22, 43]. Extensions of the Kappa distribution have been proposed and actively studied, such as the Kappa distribution with a high-energy cutoff and the distribution with a loss-cone [38, 40, 41]. In the solar wind, electron VDFs often have Kappa-type and other subcomponents [48]. In addition, ion VDFs often contain a ring- or shell-shaped “pickup” component that originates from interstellar neutral atoms [27, 62]. A shell-shaped VDF further evolves to a filled-shell VDF, due to an adiabatic expansion of the solar wind. In the presence of pickup ions (PUIs), local plasma processes can be substantially modified [24, 29, 33]. Associated with electron heating, flattop-type VDFs are often observed in and around the magnetosphere [12, 30, 34, 37, 42]. Indeed, a wide variety of VDFs are recognized throughout the heliosphere.

Particle-in-cell (PIC) simulation [7, 15] is very useful for exploring kinetic processes in plasma systems. Without PIC simulation, it is virtually impossible to accurately predict wave-particle interaction, pitch-angle scattering, and particle acceleration in the aforementioned VDFs. For a Maxwell distribution, one can use a built-in procedure to generate a normal distribution or one can use the *Box-Muller* [8] method. However, it is not always clear how to generate non-Maxwellian VDFs in simulation. For example, despite its importance, numerical procedures for Kappa distributions have been largely unknown to the community, until *Abdul & Mace* [1, 2] used its relation to Student’s  $t$  distributions. More recently, *Zenitani & Nakano* [56, 57] proposed numerical procedures for Kappa, relativistic, and loss-cone distributions. Their methods rely on only three types of basic random numbers: uniform, normal, and gamma random numbers.

Yet, there are many other VDFs that simulation scientists would like to use, as discussed later in this article. To generate such distributions, one may consider general-purpose methods such as acceptance-rejection sampling or inverse transform sampling. In the acceptance-rejection method, we need to define a good envelope function to make the rejection process efficient; otherwise the algorithm becomes increasingly inefficient, especially in three dimensions. The inverse transform method relies on the inverse of the cumulative distribution function (CDF), which is not always available analytically. Moreover, it is difficult to extend the method to multiple dimensions. Considering the limitations of these general-purpose methods, it is necessary to develop dedicated numerical procedures for a variety of non-Maxwellian VDFs in heliophysics.

---

<sup>\*</sup> seiji.zenitani@oeaw.ac.at

The purpose of this paper is to comprehensively present numerical procedures for generating non-Maxwellian VDFs in particle simulations, that are not covered by our recent studies [56, 57]. We provide “numerical recipes” for nine different distributions, in the hope that they make kinetic modeling of plasma processes easier than before. The rest of the paper is organized as follows. In Section II, we summarize random number generators for basic probability distributions in statistics. Section III discusses the  $(r, q)$  distribution that generalizes the Kappa and flattop distributions. A gamma-distribution method and a piecewise rejection method are evaluated in the 2-D parameter space. Section IV discusses the regularized Kappa distribution. Two rejection methods, a post-rejection method and a piecewise rejection method are proposed. Section V develops a procedure for a subtracted Kappa distribution, a recently-proposed Kappa loss-cone (KLC) model with a narrow loss cone. Section VI discusses ring and shell distributions with finite Gaussian width. Two methods are briefly presented. Section VII presents ring and shell Maxwellians. In particular, we introduce a shell Maxwell distribution as a handy alternative to the conventional shell distribution. Section VIII presents other isotropic distributions. The super Gaussian distribution and the filled-shell distributions are discussed. Section IX validates numerical accuracies of the proposed methods for all the distributions. Section X contains a discussion and summary.

## II. BASIC STATISTICAL DISTRIBUTIONS

### A. Exponential distribution

The exponential distribution is defined in  $0 \leq x < \infty$ . Its probability density is given by

$$\text{Exp}(x; \lambda) = \frac{1}{\lambda} \exp\left(-\frac{x}{\lambda}\right) \quad (1)$$

Here the parameter  $\lambda$  controls the scale length in  $x$ . As well known, a random number that follows the exponential distribution can be obtained by  $-\lambda \log U$ , by using a uniform random number  $U \in (0, 1]$ . One can use  $-\lambda \log(1 - U)$  instead, when  $U$  is defined in  $[0, 1)$ .

### B. Gamma distribution

The gamma distribution is one of the most important probability distributions. The probability density  $\text{Ga}(x)$  is defined in  $0 \leq x < \infty$ :

$$\text{Ga}(x; k, \lambda) = \frac{x^{k-1}}{\Gamma(k)\lambda^k} \exp\left(-\frac{x}{\lambda}\right) \quad (2)$$

Here,  $\Gamma(x)$  is the gamma function. The distribution is parameterized by the shape parameter  $k$  and the scale parameter  $\lambda$ . The exponential distribution is a special case of the gamma distribution, i.e.,  $\text{Exp}(x; \lambda) = \text{Ga}(x; 1, \lambda)$ . To generate a random number drawn from a gamma distribution, which we call a gamma variate, we may use random number generators offered by the system. If gamma generators are unavailable or if we want to make our code portable, we can implement gamma generators by using state-of-art algorithms. Depending on the shape parameter  $k$ , we have the following choices:

- For  $k > 1$ , Marsaglia & Tsang [23]’s algorithm is the de-facto standard. There are simpler methods for integer and half-integer cases (Kroese *et al.* [18], Yotsuji [53]. See also Zenitani & Nakano [56, Appendix A]).
- For  $k = 1$ , the distribution is equivalent to the exponential distribution. We can use the simple procedure, as discussed in Sec. II A.
- For  $k < 1$ , several acceptance-rejection methods have been developed [e.g., 3, 6]. Based on our experience, we recommend either Devroye [9, Chapter VII, Sec. 2.6] or Zenitani [59] methods.

In this paper, we denote  $X_{\text{Ga}(k, \lambda)}$  as a gamma variate with the parameters  $k, \lambda$ .

### C. Generalized beta-prime distribution

The generalized beta-prime distribution is defined in the following way. The four parameters need to be positive.

$$B'(x; \alpha, \beta, \gamma, \delta) = \frac{\gamma \Gamma(\alpha + \beta)}{\delta^{\alpha \gamma} \Gamma(\alpha) \Gamma(\beta)} \left(1 + \left(\frac{x}{\delta}\right)^\gamma\right)^{-(\alpha + \beta)} x^{\alpha \gamma - 1} \quad (3)$$

A beta-prime variate can be obtained from two gamma variates [56, Section III].

$$X_{B'(\alpha, \beta, \gamma, \delta)} = \delta \left( \frac{X_{\text{Ga}(\alpha, \epsilon)}}{X_{\text{Ga}(\beta, \epsilon)}} \right)^{1/\gamma} \quad (4)$$

#### D. Student's $t$ distribution

Student's  $t$  distribution is defined by

$$\text{St}(\mathbf{x}; \nu, \sigma, p) d\mathbf{x} = \frac{1}{(\pi \nu \sigma^2)^{p/2}} \frac{\Gamma[(\nu + p)/2]}{\Gamma(\nu/2)} \left( 1 + \frac{1}{\nu} \frac{\mathbf{x}^2}{\sigma^2} \right)^{-\frac{(\nu+p)}{2}} d\mathbf{x} \quad (5)$$

where  $\nu$  is degree of freedom,  $p$  is the dimension, and  $\mathbf{x}$  is a multi-dimensional ( $p$ -dimensional) variable. Such a  $t$ -variate  $\mathbf{x}$  can be obtained by

$$\mathbf{x} = \sqrt{\nu \sigma^2} \frac{\mathbf{n}}{\sqrt{X_{\text{Ga}(\nu/2, 2)}}}, \quad (6)$$

where  $\mathbf{n}$  is a  $p$ -dimensional normal variate. Eq. (6) is identical to a well-known procedure with a chi-squared variate [18, 53], because the gamma distribution  $\text{Ga}(\nu/2, 2)$  is equivalent to the chi-squared distribution with  $\nu$  degrees of freedom.

### III. $(r, q)$ DISTRIBUTION

The generalized  $(r, q)$  distribution was proposed to model flattop-type non-Maxwellian VDFs [36, 54]. It often draws attention in and around the terrestrial magnetosphere [e.g., 34, 35, 37]. The phase space density of the distribution is defined as follows:

$$f_{\text{rq}}(\mathbf{v}; r, q, \theta_{\parallel}, \theta_{\perp}) d^3v = N_0 \cdot C_{\text{rq}} \left( 1 + \frac{1}{q-1} \left( \frac{v_{\parallel}^2}{\theta_{\parallel}^2} + \frac{v_{\perp}^2}{\theta_{\perp}^2} \right)^{1+r} \right)^{-q} d^3v, \quad (7)$$

$$C_{\text{rq}} = \frac{3\Gamma(q)}{4\pi(q-1)^{\frac{3}{2(1+r)}} \theta_{\parallel} \theta_{\perp}^2 \Gamma\left(1 + \frac{3}{2(1+r)}\right) \Gamma\left(q - \frac{3}{2(1+r)}\right)}, \quad (8)$$

where  $N_0$  is the plasma number density,  $C_{\text{rq}}$  is the normalization constant, and  $\theta_{\parallel}$  and  $\theta_{\perp}$  are characteristic speeds in the parallel and perpendicular directions with respect to the magnetic field. We consider  $r > -1$  and  $q > 1$ . The pressures and the kinetic energy density of the distribution are

$$P_{\parallel} = \frac{1}{3} N_0 m \theta_{\parallel}^2 K_{\text{rq}}, \quad P_{\perp} = \frac{1}{3} N_0 m \theta_{\perp}^2 K_{\text{rq}}, \quad \mathcal{E} = \frac{1}{6} N_0 m \left( \theta_{\parallel}^2 + 2\theta_{\perp}^2 \right) K_{\text{rq}}, \quad (9)$$

$$K_{\text{rq}} = (q-1)^{\frac{1}{2(1+r)}} \frac{\Gamma\left(\frac{5}{2(1+r)}\right) \Gamma\left(q - \frac{5}{2(1+r)}\right)}{\Gamma\left(\frac{3}{2(1+r)}\right) \Gamma\left(q - \frac{3}{2(1+r)}\right)} \quad (10)$$

To keep these second velocity moments finite, the parameters must satisfy:

$$q - \frac{5}{2(1+r)} > 0. \quad (11)$$

The phase space density (Eq. (7)) with  $(r, q, \theta_{\parallel}, \theta_{\perp}) = (2, 2, \theta, \theta)$  is shown by the black line in Figure 1(a). The distribution gives a flattop-like picture.

The  $(r, q)$  distribution reverts to the (bi-)Kappa distribution [22, 31, 46] when  $r = 0$ ,  $q = \kappa + 1$ .

$$\begin{aligned} f_{\kappa}(\mathbf{v}; \kappa, \theta_{\parallel}, \theta_{\perp}) d^3v &= f_{\text{rq}}(\mathbf{v}; 0, \kappa + 1, \theta_{\parallel}, \theta_{\perp}) d^3v \\ &= \frac{1}{(\pi \kappa)^{3/2} \theta_{\parallel} \theta_{\perp}^2} \frac{\Gamma(\kappa + 1)}{\Gamma(\kappa - 1/2)} \left( 1 + \frac{1}{\kappa} \left( \frac{v_{\parallel}^2}{\theta_{\parallel}^2} + \frac{v_{\perp}^2}{\theta_{\perp}^2} \right) \right)^{-(\kappa+1)} d^3v \end{aligned} \quad (12)$$

The distribution also reverts to a popular form of the (bi-)flattop distribution [30, 42, 58] when  $r = \kappa - 1$  and  $q = 1 + 1/\kappa$ . Below,  $\bar{\theta} = \kappa^{-1/2\kappa}\theta$  is the characteristic flattop speed.

$$f_{\text{ft}}(\mathbf{v}; \kappa, \theta_{\parallel}, \theta_{\perp}) d^3v = f_{\text{rq}}(\mathbf{v}; \kappa - 1, 1 + 1/\kappa, \theta_{\parallel}, \theta_{\perp}) d^3v \\ = \frac{3N_0}{4\pi\bar{\theta}_{\parallel}\bar{\theta}_{\perp}^2} \frac{\Gamma(1 + \frac{1}{\kappa})}{\Gamma(1 + \frac{3}{2\kappa})\Gamma(1 - \frac{1}{2\kappa})} \left(1 + \left(\frac{v_{\parallel}^2}{\bar{\theta}_{\parallel}^2} + \frac{v_{\perp}^2}{\bar{\theta}_{\perp}^2}\right)^{\kappa}\right)^{-(\kappa+1)/\kappa} d^3v, \quad (13)$$

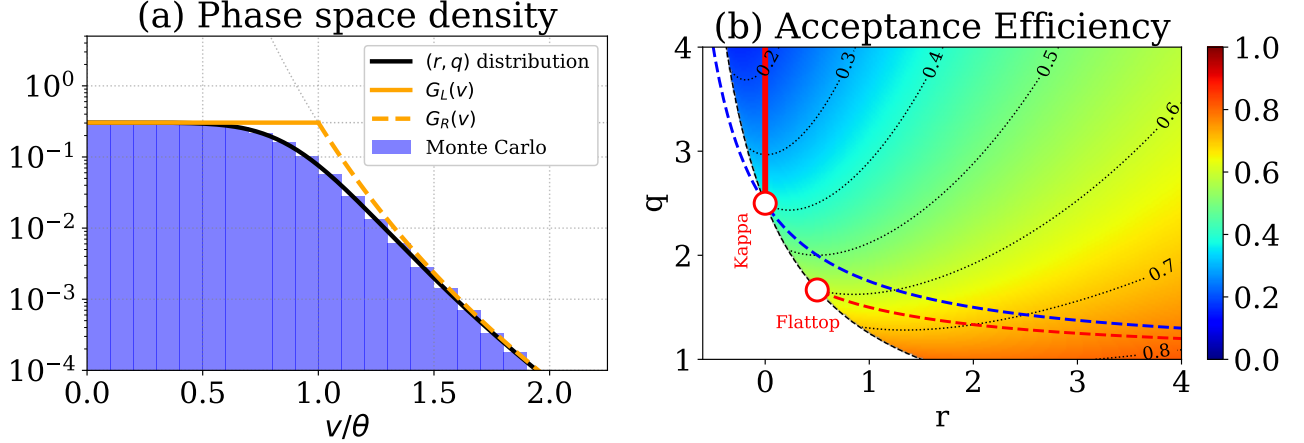


FIG. 1. (a) Phase space density of the  $(r, q)$  distribution with  $(r, q, \theta_{\parallel}, \theta_{\perp}) = (2, 2, \theta, \theta)$ . The distribution function (black line; Eq. (7)) and normalized Monte Carlo results (blue histogram) of  $10^6$  particles. The solid and dashed orange lines show the left and right envelope functions (Eq. (17)). (b) Acceptance efficiency for the  $(r, q)$  distribution (Eq. (20)). The vertical red line corresponds to the Kappa distribution and the red dashed line corresponds to the flattop distribution. Below the blue dashed line, the beta-prime method requires a gamma distribution with a shape parameter less than unity in the denominator.

Next, we discuss a random number generation for the  $(r, q)$  distribution. For a moment, we assume  $\theta_{\parallel} = \theta_{\perp} = \theta$ . To help our discussion, we consider a radial distribution in spherical coordinates,

$$F_{\text{rq}}(v)dv = f_{\text{rq}}(v)4\pi v^2 dv \quad (14)$$

One can translate Eq. (14) into the generalized beta-prime distribution (Eq. (3)),

$$F_{\text{rq}}(v) = N_0 B' \left( v; \frac{3}{2(1+r)}, q - \frac{3}{2(1+r)}, 2(1+r), (q-1)^{\frac{1}{2(1+r)}}\theta \right). \quad (15)$$

From Eq. (4), we can obtain the radial velocity  $v$  by using two gamma variates,

$$v = (q-1)^{\frac{1}{2(1+r)}}\theta \left( \frac{X_{\text{Ga}}(\frac{3}{2(1+r)}, 1)}{X_{\text{Ga}}(q - \frac{3}{2(1+r)}, 1)} \right)^{\frac{1}{2(1+r)}} = \theta \left( (q-1) \frac{X_{\text{Ga}}(\frac{3}{2(1+r)}, 1)}{X_{\text{Ga}}(q - \frac{3}{2(1+r)}, 1)} \right)^{\frac{1}{2(1+r)}} \quad (16)$$

After obtaining  $v$ , we need to scatter the vector in random directions in 3D, by using two uniform variates  $U_1, U_2 \sim U(0, 1)$ . We can easily extend it for  $\theta_{\parallel} \neq \theta_{\perp}$ . The procedure is presented in Algorithm 3.1 in Table I. Caution is needed when  $q \leq 1 + \frac{3}{2(1+r)}$ . In such a case, the gamma distribution in the denominator of Eq. (16) has the shape parameter  $k = q - \frac{3}{2(1+r)}$  less than unity. As the gamma distribution with shape less than unity has a non-zero density at  $v = 0$ , we need to take care of the division by zero in Eq. (16).

We present another procedure, the piecewise rejection method, for generating the  $(r, q)$  distribution. We employ the following piecewise envelope functions.

$$G(v) = \begin{cases} G_L(v) = C_{\text{rq}} & (0 \leq v < v_c) \\ G_R(v) = C_{\text{rq}} \left\{ \frac{1}{q-1} \left( \frac{v}{\theta} \right)^{2(1+r)} \right\}^{-q} & (v_c \leq v < \infty) \end{cases} \quad (17)$$

TABLE I. Sampling algorithms for the  $(r, q)$  distribution

<b>Algorithm 3.1: Beta-prime method</b>
generate $X_1 \sim \text{Ga}(\frac{3}{2(1+r)}, 1)$
generate $X_2 \sim \text{Ga}(q - \frac{3}{2(1+r)}, 1)$
generate $U_1, U_2 \sim U(0, 1)$
$x \leftarrow [(q-1)X_1/X_2]^{\frac{1}{2(1+r)}}$
$v_{\parallel} \leftarrow \theta_{\parallel} x (2U_1 - 1)$
$v_{\perp 1} \leftarrow 2\theta_{\perp} x \sqrt{U_1(1-U_1)} \cos(2\pi U_2)$
$v_{\perp 2} \leftarrow 2\theta_{\perp} x \sqrt{U_1(1-U_1)} \sin(2\pi U_2)$
<b>return</b> $v_{\parallel}, v_{\perp 1}, v_{\perp 2}$
<b>Algorithm 3.2: Piecewise rejection method</b>
$p_2 \leftarrow \frac{3}{2q(1+r)}, p_1 \leftarrow 1 - p_2, R \leftarrow (q-1)^{\frac{1}{2(1+r)}}$
<b>repeat</b>
generate $U_1, U_2 \sim U(0, 1)$
<b>if</b> $U_1 \leq p_1$ <b>then</b>
$x \leftarrow (U_1/p_1)^{1/3}$
<b>if</b> $U_2 < (1+x^{2(1+r)})^{-q}$ , <b>break</b>
<b>else</b>
$x \leftarrow ((1-U_1)/p_2)^{\frac{1}{3-2q(1+r)}}$
<b>if</b> $U_2 < (x^{-2(1+r)} + 1)^{-q}$ , <b>break</b>
<b>endif</b>
<b>end repeat</b>
generate $U_3, U_4 \sim U(0, 1)$
$v_{\parallel} \leftarrow \theta_{\parallel} Rx (2U_3 - 1)$
$v_{\perp 1} \leftarrow 2\theta_{\perp} Rx \sqrt{U_3(1-U_3)} \cos(2\pi U_4)$
$v_{\perp 2} \leftarrow 2\theta_{\perp} Rx \sqrt{U_3(1-U_3)} \sin(2\pi U_4)$
<b>return</b> $v_{\parallel}, v_{\perp 1}, v_{\perp 2}$

In Figure 1(a), the solid and dashed orange lines indicate the two envelopes in this case. The left and right envelopes meet at  $v \equiv v_c = (q-1)^{1/2(1+r)}\theta$ . In the radial direction in spherical coordinates, they give the following two areas,

$$S_L = \int_0^{v_c} G_L(v) 4\pi v^2 dv = \frac{4\pi C_{\text{rq}} v_c^3}{3} \quad (18)$$

$$S_R = \int_{v_c}^{\infty} G_R(v) 4\pi v^2 dv = \frac{4\pi C_{\text{rq}} v_c^3}{2q(1+r) - 3}. \quad (19)$$

Using the fact that their ratio is  $[2q(1+r) - 3] : 3$ , we can construct a rejection scheme, as shown in Algorithm 3.2 (Table I). We split the logical flow at this ratio. Then, comparing the distribution function and the envelope functions, we carry out the rejection procedure. Trivial modifications for  $\theta_{\parallel} \neq \theta_{\perp}$  are also included in the procedure. The acceptance efficiency is estimated to be

$$\text{eff}_{\text{rq}} = \frac{1}{S_L + S_R} = \frac{\Gamma\left(1 + \frac{3}{2(1+r)}\right) \Gamma\left(1 + q - \frac{3}{2(1+r)}\right)}{\Gamma(1+q)} \quad (20)$$

The efficiency is shown by a colormap in the  $(r, q)$  parameter space in Figure 1(b). The distribution is undefined in the lower-left empty region, where Eq. (11) is not satisfied. Along the vertical red line, the  $(r, q)$  distribution corresponds to the Kappa distribution (Eq. (12)). The dashed red line corresponds to the flattop distribution (Eq. (13)). The efficiency for the flattop distribution is given by

$$\text{eff}_{\text{ft}} = \frac{\Gamma\left(1 + \frac{3}{2\kappa}\right) \Gamma\left(2 - \frac{1}{2\kappa}\right)}{\Gamma\left(2 + \frac{1}{\kappa}\right)} > \frac{3}{5} \quad (\text{for } \kappa > 3/2). \quad (21)$$

Practically, one can generate the  $(r, q)$  distribution by using either of the two methods. The piecewise rejection method can be easily implemented, but it becomes increasingly inefficient in a Kappa-like regime in the upper-left in Figure 1(b). In such cases, the beta-prime method is favorable. Along the red line, one should use dedicated methods for the Kappa distribution [2, 56, 60]. Below the blue curve in Figure 1(b),  $q \leq 1 + \frac{3}{2(1+r)}$ , we recommend the piecewise rejection method, because the beta-prime method may encounter the zero-division problem. Using Algorithm 3.1, we have numerically generated  $10^6$  particles that follows the  $(r, q)$  distribution with  $(r, q) = (2, 2)$ . Their distribution is shown by the blue histogram in Figure 1(a). The numerical results are in excellent agreement with Eq. (7).

#### IV. REGULARIZED KAPPA DISTRIBUTION

The regularized Kappa distribution [38] is essentially a Kappa distribution with a high-energy cutoff. Since higher-order velocity moments no longer diverges, we can use the kappa index of  $0 < \kappa < 3/2$  that are not accessible in the standard Kappa distribution. Owing to these and other reasons, the regularized Kappa distribution has attracted recent attention [20]. It is defined in the following way.

$$f_{\text{rk}}(\mathbf{v}; \kappa, \theta, \alpha) d^3v = \frac{N_0}{(\pi \kappa \theta^2)^{3/2} \mathcal{U}(\frac{3}{2}, \frac{3}{2} - \kappa, \alpha^2 \kappa)} \left(1 + \frac{v^2}{\kappa \theta^2}\right)^{-(\kappa+1)} \exp\left(-\alpha^2 \frac{v^2}{\theta^2}\right) d^3v \quad (22)$$

where  $\kappa$  is the spectral index,  $\theta$  is the characteristic velocity,  $\alpha$  is a cut-off parameter, and

$$\mathcal{U}(a, b, z) = \frac{1}{\Gamma(a)} \int_0^\infty x^{a-1} (1+x)^{b-a-1} e^{-zx} dx \quad (23)$$

is Kummer's U-function (Tricomi function). The cut-off parameter is usually set to be small,  $\alpha \ll 1$ . For convenience, we limit our attention to  $0 \leq \alpha < 1$ . The energy density is given by the combination of the U-functions [39].

$$\mathcal{E} = \int f_{\text{rk}}(\mathbf{v}; \kappa, \alpha) \left(\frac{1}{2} m v^2\right) d^3v = \frac{3}{4} N_0 m \kappa \theta^2 \frac{\mathcal{U}(\frac{5}{2}, \frac{5}{2} - \kappa, \alpha^2 \kappa)}{\mathcal{U}(\frac{3}{2}, \frac{3}{2} - \kappa, \alpha^2 \kappa)} \quad (24)$$

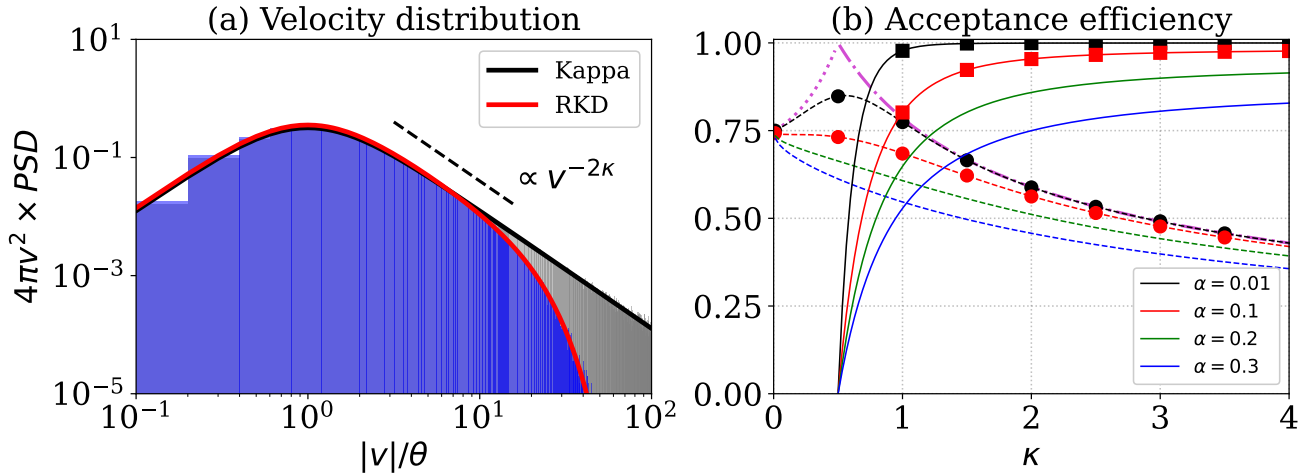


FIG. 2. (a) Radial velocity distribution of the regularized Kappa distribution. The distribution function with  $(\kappa, \theta, \alpha) = (1, 1, 0.05)$  (red line; Eq. (22)) is compared with numerical results of  $10^6$  particles (blue histogram). For reference, the standard Kappa distribution  $(\kappa, \theta, \alpha) = (1, 1, 0)$  (black line; Eq. (12)) and normalized numerical results of  $10^6$  particles (gray histogram) are presented. (b) Acceptance efficiency. The theory (solid lines; Eq. (28)) and numerical results (squares) of the post-rejection method, and the theory (dashed lines; Eq. (37)) and numerical results (circles) of the piecewise rejection method are presented. The dash-dotted and dotted purple lines indicate upper-bounds (Eqs. (38) and (39)).

An omni-directional distribution  $4\pi v^2 f_{\text{rk}}(v)$  for  $(\kappa, \theta, \alpha) = (1, 1, 0.05)$  is presented by the red line in Figure 2(a). The distribution of a standard Kappa distribution with  $(\kappa, \theta, \alpha) = (1, 1, 0)$  is also presented by the black line. One can see

power-law slopes of the Kappa distributions, with index  $\sim -2\kappa$ . The density of the regularized Kappa distribution drops beyond the cut-off velocity of  $v_c = \theta/\alpha = 20\theta$ . It has three characteristic energy ranges: the thermal core ( $0 < v < \theta$ ), the power-law slope ( $\theta < v \lesssim v_c$ ), and the high-energy cutoff ( $v \approx v_c$ ). Note that the standard Kappa distribution with  $\kappa = 1$  is undefined, because its energy density goes to infinity for  $\kappa \leq 3/2$ . However, we can still calculate the density of the standard Kappa distribution for  $\kappa > 1/2$ .

We propose two rejection methods to generate the regularized Kappa distribution in PIC simulation. We first introduce a post-rejection method. By setting  $N_0 = 1$ , we rewrite Eq. (22) in the following way,

$$f_{\text{rk}}(\mathbf{v}; \kappa, \theta, \alpha) d^3v = \left( \frac{\Gamma(\kappa - 1/2)}{\mathcal{U}(\frac{3}{2}, \frac{3}{2} - \kappa, \alpha^2 \kappa) \Gamma(\kappa + 1)} \right) \times \left\{ f_\kappa(\mathbf{v}; \kappa, \theta, \theta) \right\} \times \exp\left(-\frac{\alpha^2 v^2}{\theta^2}\right) d^3v \quad (25)$$

In the right hand side, the first bracketed term is a constant, the second curly-bracketed term stands for the Kappa distribution (Eq. (12)), and the last exponential term ranges from zero to unity. So, we generate the Kappa distribution first. The distribution is equivalent to a multivariate  $t$ -distribution (Eq. (5)), i.e.,

$$f_\kappa(\mathbf{v}; \kappa, \theta, \theta) d^3v = \text{St}\left(\mathbf{v}; 2\kappa - 1, \sqrt{\frac{\kappa \theta^2}{2\kappa - 1}}, 3\right) d^3v \quad (26)$$

and then we can use a Monte Carlo method, prescribed by Eq. (6) [2, 56]. After generating the Kappa distribution, we further apply the rejection method. We take the result, if a uniform variate  $U \sim U(0, 1)$  satisfy

$$U < \exp\left(-\frac{\alpha^2 v^2}{\theta^2}\right), \quad (27)$$

If this is not met, we discard the result. The final velocity distribution follows Eq. (22). The entire procedure is summarized in Algorithm 4.1 in Table II. The acceptance efficiency is given by an reciprocal of the bracketed term in Eq. (25).

$$\text{eff}_{\text{rk}}(\kappa, \alpha) = \frac{\mathcal{U}(\frac{3}{2}, \frac{3}{2} - \kappa, \alpha^2 \kappa) \Gamma(\kappa + 1)}{\Gamma(\kappa - 1/2)} \quad (28)$$

When  $\alpha \rightarrow 0$ , the rejection is rarely used, and the efficiency approaches  $\text{eff}_{\text{rk}}(\kappa, 0) \rightarrow 1$ .

Next, we propose another procedure, the piecewise rejection method. Again we set  $N_0 = 1$ . Using  $x = v^2/(\kappa \theta^2)$ , we consider a distribution of  $x$ , i.e.,  $g(x)$ .

$$g(x) \equiv f_{\text{rk}}(v) 4\pi v^2 \left| \frac{dv}{dx} \right| = c_{\text{rk}} \cdot x^{1/2} (1+x)^{-(\kappa+1)} \exp(-\alpha^2 \kappa x) \quad (29)$$

$$c_{\text{rk}} = \frac{2}{\sqrt{\pi} \mathcal{U}(\frac{3}{2}, \frac{3}{2} - \kappa, \alpha^2 \kappa)} \quad (30)$$

Here,  $c_{\text{rk}}$  is a constant. We will develop a Monte Carlo procedure for  $g(x)$ . We consider the following envelope functions,

$$G(x) = \begin{cases} G_L(x) = c_{\text{rk}} (1+x)^{-\kappa-1/2} & (0 \leq x < x_c) \\ G_R(x) = c_{\text{rk}} x_c^{1/2} (1+x_c)^{-(\kappa+1)} \exp(-x/x_c) & (x_c \leq x < \infty) \end{cases} \quad (31)$$

where  $x_c = 1/(\alpha^2 \kappa)$  is a cutoff value. One can see  $g(x) < G_L(x)$  for  $0 \leq x$ . In addition, since  $\alpha < 1$ , the following  $x$ -derivative is negative for  $(1/\kappa) < x_c \leq x$ ,

$$\frac{\partial}{\partial x} \left( x^{1/2} (1+x)^{-(\kappa+1)} \right) = \frac{1 - \kappa x}{2x^{1/2}(1+x)^{\kappa+2}} < 0 \quad (32)$$

This ensures  $g(x) < G_R(x)$  for  $x_c \leq x$ . The areas below the envelopes are given by

$$S_L = \int_0^{x_c} G_L(x) dx = \begin{cases} c_{\text{rk}} \frac{2}{1-2\kappa} \left( (1+x_c)^{1/2-\kappa} - 1 \right) & (\kappa \neq 1/2) \\ c_{\text{rk}} \log(1+x_c) & (\kappa = 1/2) \end{cases} \quad (33)$$

$$S_R = \int_{x_c}^{\infty} G_R(x) dx = c_{\text{rk}} \frac{1}{e} x_c^{3/2} (1+x_c)^{-(\kappa+1)} \quad (34)$$

TABLE II. Algorithms for the regularized Kappa distribution

where  $e = 2.718\ldots$  is the Euler number. Examining integral forms of the envelope functions, we can construct inverse transform procedures to generate the envelope distributions. For example, when  $\kappa \neq 1/2$ , for the left area  $S_L$ , we equate a uniform variate  $u \sim U(0, 1)$

$$\left( (1+x)^{1/2-\kappa} - 1 \right) = u \left( (1+x_c)^{1/2-\kappa} - 1 \right) \quad (35)$$

and then we find the following inverse transform procedure

$$x \leftarrow [u(1+x_c)^{1/2-\kappa} + (1-u)]^{\frac{1}{1/2-\kappa}} - 1. \quad (36)$$

Then, we construct rejection conditions, by comparing the distribution (Eq. (29)) and the envelope functions (Eq. (31)). After obtaining  $x$ , we recover  $v$  from  $x$ . Then we randomly scatter  $v$  into three directions. The entire procedure is shown in Algorithm 4.2 in Table II. The procedure does not contain the coefficient  $c_{rk}$ , because it is

cancelled away. The acceptance efficiency is given by the reciprocal of the total area.

$$\text{eff}_{\text{rk2}}(\kappa, \alpha) = \frac{1}{S_L + S_R} = \frac{\sqrt{\pi} \mathcal{U}\left(\frac{3}{2}, \frac{3}{2} - \kappa, \alpha^2 \kappa\right)}{2 \left( \frac{2}{1-2\kappa} \left( (1+x_c)^{1/2-\kappa} - 1 \right) + \frac{1}{e} x_c^{3/2} (1+x_c)^{-(\kappa+1)} \right)} \quad (37)$$

We have carried out Monte Carlo tests of our procedures in Table II. Using  $10^6$  particles, we have generated the regularized Kappa distribution  $((\kappa, \theta, \alpha) = (1, 1, 0.05))$  by the piecewise rejection method (Algorithm 4.2), and then the particle distribution is shown by the blue histogram in Figure 2(a). The distribution is in excellent agreement with the exact solution (the red line). We have also generated the standard Kappa distribution  $((\kappa, \theta, \alpha) = (1, 1, 0))$  by the post-rejection method (Algorithm 4.1), and their distribution is shown by the gray histogram. It agrees with the exact solution (the black line).

Figure 2(b) shows the acceptance efficiency of the two methods. The solid and dashed lines present theoretical predictions for the post-rejection method (Eq. (28)) and for the piecewise rejection method (Eq. (37)), respectively. Several  $\alpha$  values are indicated by color. The squares and the circles are numerical results, in agreement with the predictions.

The post-rejection method can be used for  $\kappa > 1/2$ , because it relies on the standard Kappa distribution. At  $\kappa$  approaches  $1/2$ , the density in the power-law tail of the standard Kappa distribution goes to infinity. The density beyond the cutoff velocity diverges, and then the acceptance efficiency drops to zero. One may recall that the standard Kappa distribution is defined for  $\kappa > 3/2$ , where the second velocity moment remains finite. For  $1/2 < \kappa \leq 3/2$ , the energy of the standard Kappa distribution diverges, but we can still compute its density. Then, by applying the rejection method, both the density and energy density of the regularized Kappa distribution remain finite. As  $\kappa$  increases, the efficiency becomes better. This is because the power-law tail becomes less pronounced for large  $\kappa$ , and because there are fewer particles beyond the cutoff velocity. By definition, the efficiency of the post-rejection method approaches unity in the  $\alpha \rightarrow 0$  limit. For  $\alpha = 0.01$  (the black line and the black squares), the acceptance efficiency is almost unity, because of a very high cutoff velocity ( $v_c = 100\theta$ ). For  $\alpha = 0.1$  (the red line and the red squares), or when the cutoff velocity is  $v \gtrsim v_c = 10\theta$ , the acceptance efficiency is greater than 95% for  $\kappa > 2$ . As  $\alpha$  increases, the algorithm becomes increasingly inefficient. The  $\alpha \gtrsim 1$  regime is unimportant, and out of the scope of this paper. Technically, as shown in Table II, the post-rejection method is simple, and easy to implement. The method requires caution when  $1/2 < \kappa \leq 3/2$ . As described in Section II D and in Algorithm 4.1, the Kappa generator (the  $t$ -generator) uses one gamma variate. When  $1/2 < \kappa \leq 3/2$ , it has the scale parameter less than unity, i.e.,  $\kappa - 1/2 \leq 1$ . In such a case, the gamma distribution ( $\text{Ga}(x)$ ) has non-zero density at  $x = 0$ . This may cause a zero-division problem in the algorithm.

The piecewise rejection method works in the entire range of  $\kappa \geq 0$ . When  $\kappa = 1/2$ , we need to switch some procedures, but they are fully described in Algorithm 4.2 in Table II. Its efficiency is moderate. It is not unity in the  $\alpha \rightarrow 0$  limit. When  $\alpha \rightarrow +0$  and  $\kappa > 1/2$ , from Eqs. (29) and (31), we find

$$\text{eff}_{\text{rk2}}(\kappa, 0) \approx \frac{\int_0^\infty x^{1/2} (1+x)^{-\kappa-1} dx}{\int_0^\infty (1+x)^{-\kappa-1/2} dx} = \frac{\frac{\sqrt{\pi} \Gamma(\kappa - \frac{1}{2})}{2 \Gamma(\kappa+1)} \int_0^\infty B' \left( x; \frac{3}{2}, \kappa - \frac{1}{2}, 1, 1 \right) dx}{1/(\kappa - 1/2)} = \frac{\sqrt{\pi} \Gamma(\kappa + \frac{1}{2})}{2 \Gamma(\kappa+1)} \quad (38)$$

where we utilized the beta-prime distribution (Eq. (3)). When  $\alpha \rightarrow +0$  and  $0 < \kappa < 1/2$ , Eq. (37) can be approximated to

$$\text{eff}_{\text{rk2}}(\kappa, 0) \approx \frac{\sqrt{\pi} \mathcal{U}\left(\frac{3}{2}, \frac{3}{2} - \kappa, \frac{1}{x_c}\right)}{2 \left( \frac{2}{1-2\kappa} + \frac{1}{e} \right) x_c^{1/2-\kappa}} \approx \frac{\Gamma(1/2 - \kappa)}{\left( \frac{2}{1-2\kappa} + \frac{1}{e} \right)} \quad (39)$$

with help from the asymptotic relation for  $x_c \rightarrow \infty$  [32, Section 13, 13.2.18],

$$\mathcal{U}\left(\frac{3}{2}, \frac{3}{2} - \kappa, \frac{1}{x_c}\right) \approx \frac{\Gamma(1/2 - \kappa)}{\Gamma(3/2)} x_c^{1/2-\kappa} + \frac{\Gamma(\kappa - 1/2)}{\Gamma(\kappa+1)} + \mathcal{O}\left(x_c^{-1/2-\kappa}\right) \quad (40)$$

In Figure 2(b), the purple dot-dashed line and dotted line indicate estimates of the  $\alpha \rightarrow 0$  limit (Eqs. (38) and (39)). They give good upper bounds to the efficiency. As  $\alpha$  increases, the piecewise rejection method becomes less efficient, similarly as the post-rejection method. In the  $\kappa \rightarrow +0$  limit, the method gives similar results regardless of  $\alpha$ , because the distribution (Eq. (29)) resembles a Gamma distribution, which is scale-free.

$$g(x) \approx c_{\text{rk}} \cdot x^{-\kappa-1/2} \exp(-x/x_c) \propto \text{Ga}(x; 1/2 - \kappa, x_c) \quad (41)$$

The efficiencies converge to  $\text{eff}_{\text{rk2}}(0, 0) \approx \sqrt{\pi}/(2 + 1/e) \approx 0.7485$  as estimated by Eq. (39).

In summary, we have discussed the two methods. The piecewise rejection method is the only choice for  $0 < \kappa \leq 1/2$ . Either method can be used for  $1/2 < \kappa \leq 3/2$ , but caution is needed for the post-rejection method. For  $\kappa > 3/2$ , we recommend the post-rejection method, which outperforms the piecewise rejection method.

TABLE III. Algorithm for the subtracted Kappa distribution

---

**Algorithm 5: subtracted Kappa ( $\kappa > 3/2$ )**

---

```

generate  $U_1, U_2, U_3 \sim U(0, 1)$ 
generate  $N \sim \mathcal{N}(0, 1)$ 
generate  $Y \sim \text{Ga}(\kappa - 1/2, 2)$ 
 $x \leftarrow -\log U_1 - \beta \log \left( \min \left( \frac{U_2}{1-\Delta}, 1 \right) \right)$ 
 $v_{\perp 1} \leftarrow \theta_{\perp} \sqrt{2\kappa x} \cos(2\pi U_3) / \sqrt{Y}$ 
 $v_{\perp 2} \leftarrow \theta_{\perp} \sqrt{2\kappa x} \sin(2\pi U_3) / \sqrt{Y}$ 
 $v_{\parallel} \leftarrow \theta_{\parallel} \sqrt{\kappa N} / \sqrt{Y}$ 
return  $v_{\perp 1}, v_{\perp 2}, v_{\parallel}$ 

```

---

## V. SUBTRACTED KAPPA DISTRIBUTION

To date, several loss-cone distribution models have been developed. To control the loss-cone angle, some models use a power of the perpendicular velocity, i.e.,  $(v_{\perp})^{2j}$  [10], and others use a power of the pitch-angle sine, i.e.,  $(\sin \alpha)^{2j} = (v_{\perp}/v)^{2j}$  [17], where  $j \geq 0$  is the loss-cone index and  $\alpha$  is the pitch angle. These models are not easy to use, because a narrow loss cone in the Earth's magnetosphere requires the index less than unity. Instead, the subtracted Maxwellian distribution [5] has been widely used. It has intermediate characteristics between the *Dory et al.* [10] models with  $j = 0$  and  $j = 1$ .

The Kappa loss-cone (KLC) distributions have been studied for decades [41, 50]. Similarly, the loss-cone is approximated by a power of the perpendicular velocity [41] or the pitch-angle sine [50, 57], but it was very recently that *Summers & Stone* [40] proposed the subtracted Kappa distribution, a Kappa extension of the subtracted Maxwellian. This new model is promising for studying kinetic processes in the KLC distribution with a narrow loss-cone. The phase space density  $f_{\text{sk}}$ , its normalization constant  $C_{\text{sk}}$ , pressures, energy density, and the pressure anisotropy  $A$  are given by:

$$f_{\text{sk}}(v_{\parallel}, \mathbf{v}_{\perp}) d^3v = N_0 \cdot C_{\text{sk}} \left\{ \frac{1-\Delta\beta}{1-\beta} \left( 1 + \frac{v_{\parallel}^2}{\kappa\theta_{\parallel}^2} + \frac{v_{\perp}^2}{\kappa\theta_{\perp}^2} \right)^{-(\kappa+1)} - \frac{1-\Delta}{1-\beta} \left( 1 + \frac{v_{\parallel}^2}{\kappa\theta_{\parallel}^2} + \frac{v_{\perp}^2}{\beta\kappa\theta_{\perp}^2} \right)^{-(\kappa+1)} \right\} d^3v \quad (42)$$

$$= N_0 \cdot C_{\text{sk}} \left\{ \Delta \cdot \left( 1 + \frac{v_{\parallel}^2}{\kappa\theta_{\parallel}^2} + \frac{v_{\perp}^2}{\kappa\theta_{\perp}^2} \right)^{-(\kappa+1)} + \frac{1-\Delta}{1-\beta} \left[ \left( 1 + \frac{v_{\parallel}^2}{\kappa\theta_{\parallel}^2} + \frac{v_{\perp}^2}{\kappa\theta_{\perp}^2} \right)^{-(\kappa+1)} - \left( 1 + \frac{v_{\parallel}^2}{\kappa\theta_{\parallel}^2} + \frac{v_{\perp}^2}{\beta\kappa\theta_{\perp}^2} \right)^{-(\kappa+1)} \right] \right\} d^3v \quad (43)$$

$$C_{\text{sk}} = \frac{\Gamma(\kappa+1)}{(\kappa\pi)^{3/2} \theta_{\parallel} \theta_{\perp}^2 \Gamma(\kappa - \frac{1}{2})}, \quad (44)$$

$$P_{\parallel} = \frac{\kappa}{2\kappa-3} N_0 m \theta_{\parallel}^2, \quad P_{\perp} = \frac{\kappa(1+\beta[1-\Delta])}{2\kappa-3} N_0 m \theta_{\perp}^2, \quad (45)$$

$$\mathcal{E} = \frac{\kappa}{2\kappa-3} N_0 m \left( \frac{1}{2} \theta_{\parallel}^2 + (1+\beta[1-\Delta]) \theta_{\perp}^2 \right), \quad (46)$$

$$A \equiv \frac{P_{\perp}}{P_{\parallel}} - 1 = (1+\beta[1-\Delta]) \frac{\theta_{\perp}^2}{\theta_{\parallel}^2} - 1 \quad (47)$$

Here, the kappa index  $\kappa > 3/2$  controls a slope in the high-energy tail, the shape parameter  $\beta \in [0, 1]$  controls the opening angle of the loss cone, the filling parameter  $\Delta$  controls the density inside the loss cone, and  $\theta_{\parallel}$  and  $\theta_{\perp}$  are the parallel and perpendicular characteristic velocities. When  $\kappa \rightarrow \infty$ , the distribution reverts to the subtracted Maxwellian. When  $\beta = 0$  or  $\Delta = 1$ , it becomes a bi-Kappa distribution with no loss cone. When  $\beta = 1$ , the distribution approaches the Dory-type (Summers-type) KLC distribution with loss-cone index  $j = 1$  [41,  $\sigma = 1$  in their notation]. When  $\Delta = 0$ , the loss cone is well developed. When  $\Delta = 1$ , the loss cone is completely filled, and then the distribution reverts to a bi-Maxwellian.

Since it was proposed very recently [40], there is no Monte Carlo algorithm for the distribution. Here, we propose

a compact procedure for randomly generating the subtracted Kappa distribution in Algorithm 5 (Table III). Below, we explain why the procedure gives a random variate that is distributed by Eq. (42).

For a moment, we assume  $\Delta = 0$ . We combine two uniform variates  $U_1$  and  $U_2$  in the following way,

$$x \leftarrow -\log U_1 - \beta \log U_2 \quad (48)$$

The two terms correspond to the exponential distributions (Section II A). The probability distribution of  $x$  ( $G(x)$ ) is given by their convolution [57, Section 2].

$$G(x) = \int_0^x \left\{ \text{Exp}(s; 1) \times \text{Exp}(x - s; \beta) \right\} ds \quad (49)$$

$$= \frac{1}{1 - \beta} \left\{ \exp(-x) - \exp\left(-\frac{x}{\beta}\right) \right\} = \frac{1}{1 - \beta} e^{-x} - \frac{\beta}{1 - \beta} \left( \frac{1}{\beta} e^{-x/\beta} \right) \quad (50)$$

Eq. (50) indicates that  $G(x)$  is equivalent to the subtraction of two exponential distributions.

Next we consider three independent variates of  $E$ ,  $N$ , and  $Y$ . The first variate  $E$  follows the exponential distribution with scale  $\lambda$  (i.e.,  $E \sim \text{Exp}(\lambda)$ ),  $N$  follows the standard normal distribution (i.e.,  $N \sim \frac{1}{\sqrt{2\pi}} e^{-x^2/2}$ ), and  $Y$  follows a gamma distribution with shape  $\kappa - 1/2$  and scale 2 (i.e.,  $Y \sim \text{Ga}(\kappa - 1/2, 2)$ ). Note that we retain the scale parameter  $\lambda$  in the exponential distribution and subsequent equations. Using them, we consider the following variables.

$$V_\perp^2 = 2\theta_\perp^2 \kappa E / Y \quad (51)$$

$$V_\parallel = \theta_\parallel \sqrt{\kappa} N / \sqrt{Y} \quad (52)$$

$$Z = \frac{2}{\lambda} E + N^2 + Y \quad (53)$$

They yield the following relation and the Jacobian

$$E = \frac{V_\perp^2}{2\kappa\theta_\perp^2} Z \left( 1 + \frac{V_\parallel^2}{\kappa\theta_\parallel^2} + \frac{V_\perp^2}{\lambda\kappa\theta_\perp^2} \right)^{-1} \quad (54)$$

$$N = \frac{V_\parallel}{\sqrt{\kappa}\theta_\parallel} \sqrt{Z} \left( 1 + \frac{V_\parallel^2}{\kappa\theta_\parallel^2} + \frac{V_\perp^2}{\lambda\kappa\theta_\perp^2} \right)^{-1/2} \quad (55)$$

$$Y = Z \left( 1 + \frac{V_\parallel^2}{\kappa\theta_\parallel^2} + \frac{V_\perp^2}{\lambda\kappa\theta_\perp^2} \right)^{-1} \quad (56)$$

$$\left\| \frac{\partial(E, N, Y)}{\partial(V_\perp, V_\parallel, Z)} \right\| = \left( \left\| \frac{\partial(V_\perp, V_\parallel, Z)}{\partial(E, N, Y)} \right\| \right)^{-1} = \frac{V_\perp Z^{3/2}}{\kappa^{3/2} \theta_\parallel \theta_\perp^2} \left( 1 + \frac{V_\parallel^2}{\kappa\theta_\parallel^2} + \frac{V_\perp^2}{\lambda\kappa\theta_\perp^2} \right)^{-5/2} \quad (57)$$

Then we consider the joint probability distribution function of  $E$ ,  $N$ , and  $Y$ . It is given by a product of the exponential distribution of  $\varepsilon$ , the normal distribution of  $n$ , and the gamma distribution of  $y$ , because these three distributions are independent.

$$f_{E, N, Y}(\varepsilon, n, y) = \left( \frac{1}{w} e^{-\varepsilon/w} \right) \times \left( \frac{1}{\sqrt{2\pi}} e^{-n^2/2} \right) \times \left( \frac{y^{\kappa-3/2} e^{-y/2}}{\Gamma(\kappa - 1/2) 2^{\kappa-1/2}} \right) \quad (58)$$

Using Eqs. (54)–(57), we rewrite the joint distribution with respect to  $V_\perp$ ,  $V_\parallel$ , and  $Z$ .

$$\begin{aligned} f_{V_\perp, V_\parallel, Z}(v_\perp, v_\parallel, z) &= \frac{1}{w\sqrt{2\pi}\Gamma(\kappa - 1/2)2^{\kappa-1/2}} \left( e^{-\varepsilon/w} \right) \times \left( e^{-n^2/2} \right) \times \left( y^{\kappa-3/2} e^{-y/2} \right) \left\| \frac{\partial(E, N, Y)}{\partial(V_\perp, V_\parallel, Z)} \right\| \\ &= \left( \frac{z^\kappa e^{-z/2}}{\Gamma(\kappa + 1) 2^{\kappa+1}} \right) \times \left( 2\pi v_\perp \frac{\Gamma(\kappa + 1)}{\lambda(\pi\kappa)^{3/2} \theta_\parallel \theta_\perp^2 \Gamma(\kappa - 1/2)} \left[ 1 + \frac{v_\parallel^2}{\kappa\theta_\parallel^2} + \frac{v_\perp^2}{\lambda\kappa\theta_\perp^2} \right]^{-(\kappa+1)} \right) \end{aligned} \quad (59)$$

Eq. (59) tells us that  $Z$  is distributed by the gamma distribution with shape  $\kappa + 1$  and scale 2, i.e.,  $Z \sim \text{Ga}(\kappa + 1, 2)$ , and that the other variables  $V_\perp$  and  $V_\parallel$  are distributed by a bi-Kappa distribution (an anisotropic Kappa distribution).

These two, the gamma and the bi-Kappa distributions, are independent. In short, a procedure by Eqs. (51)–(53) gives the bi-Kappa distribution.

From Eqs. (50) and (59), we see that the procedure of Eqs. (48), (54)–(56) gives the following distribution

$$\frac{1}{1-\beta} \left( 2\pi v_{\perp} C_{\text{sk}} \left[ 1 + \frac{v_{\parallel}^2}{\kappa\theta_{\parallel}^2} + \frac{v_{\perp}^2}{\kappa\theta_{\perp}^2} \right]^{-(\kappa+1)} \right) - \frac{\beta}{1-\beta} \left( 2\pi v_{\perp} \frac{C_{\text{sk}}}{\beta} \left[ 1 + \frac{v_{\parallel}^2}{\kappa\theta_{\parallel}^2} + \frac{v_{\perp}^2}{\beta\kappa\theta_{\perp}^2} \right]^{-(\kappa+1)} \right) \quad (60)$$

$$= \frac{2\pi v_{\perp} C_{\text{sk}}}{1-\beta} \left\{ \left( 1 + \frac{v_{\parallel}^2}{\kappa\theta_{\parallel}^2} + \frac{v_{\perp}^2}{\kappa\theta_{\perp}^2} \right)^{-(\kappa+1)} - \left( 1 + \frac{v_{\parallel}^2}{\kappa\theta_{\parallel}^2} + \frac{v_{\perp}^2}{\beta\kappa\theta_{\perp}^2} \right)^{-(\kappa+1)} \right\} \quad (61)$$

We obtain the  $\Delta = 0$  case by translating  $v_{\perp} \rightarrow (v_{\perp 1}, v_{\perp 2})$ . Thus, the procedure gives the subtracted Kappa distribution when  $\Delta = 0$ .

Finally, we discuss the  $\Delta \neq 0$  cases. Like the subtracted Maxwellian, the subtracted Kappa distribution is designed as a weighted sum of the standard Kappa distribution ( $\Delta$ ) and the subtracted parts ( $1 - \Delta$ ), as shown in Eq. (43). We can generate the standard Kappa part by setting  $\beta$  to be zero. To generate a full distribution of Eq. (42), we replace Eq. (48) by the following procedure, to disable the  $\beta$  term at the probability of  $\Delta$ .

$$x \leftarrow -\log U_1 - \beta \log \left( \min \left( \frac{U_2}{1-\Delta}, 1 \right) \right) \quad (62)$$

A full recipe consists of Eqs. (62), (54)–(56), as shown in Algorithm 5 (Table III).

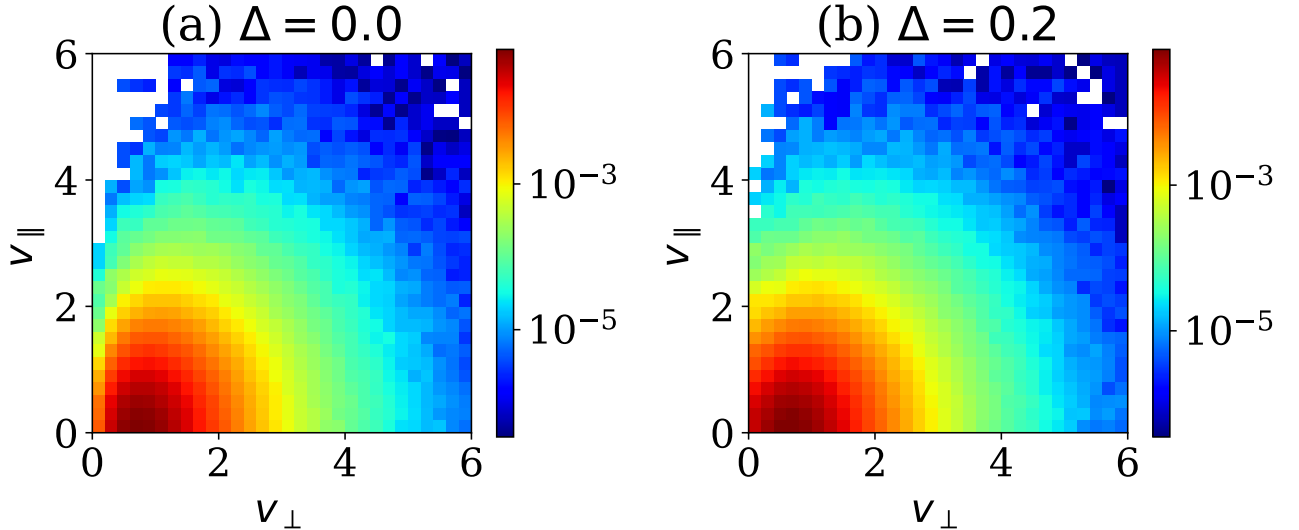


FIG. 3. Monte Carlo sampling of the subtracted Kappa distribution ( $\theta = 1.0$ ,  $\kappa = 3.5$ ,  $\beta = 0.5$ ) with  $10^6$  particles. Phase space density is shown in the  $v_{\perp}-v_{\parallel}$  plane. The filling parameter is (a)  $\Delta = 0.0$  and (b)  $\Delta = 0.2$ , respectively.

We have verified our method by a Monte Carlo test with  $10^6$  particles. Figure 3 shows the phase space density of the subtracted Kappa distribution ( $\theta = 1.0$ ,  $\kappa = 3.5$ ,  $\beta = 0.5$ ) in the  $v_{\perp}-v_{\parallel}$  plane. The filling parameters are (a)  $\Delta = 0.0$  and (b)  $\Delta = 0.2$ , respectively. We recognize a narrow loss-cone in the  $\Delta = 0.0$  case and a partially-filled loss-cone in the  $\Delta = 0.2$  case. Although not shown here, we have compared the numerical results and the exact solution at several 1-D cuts in the velocity space, and found that they are in excellent agreement.

## VI. RING AND SHELL DISTRIBUTIONS

In the solar wind, pickup ions (PUIs) lead to a ring-shaped component in the velocity space. They further evolve to an isotropic, shell-shaped distribution, because of pitch-angle scattering [47]. Considering PUI's importance in kinetic processes and their mathematical similarity, we discuss ring and shell distributions together in this section.

We first discuss a ring distribution with a Gaussian width [e.g., 19, 49]. We show the phase space density  $f_{\text{ring}}(\mathbf{v})$ , its perpendicular part  $g_{\text{ring}}(v_{\perp})$ , and an auxiliary function  $C_2(x)$ .

$$f_{\text{ring}}(\mathbf{v})d^3v = N_0 \frac{1}{\pi^{3/2} \theta_{\parallel} \theta_{\perp}^2 C_2(\frac{V}{\theta_{\perp}})} \exp \left( -\frac{v_{\parallel}^2}{\theta_{\parallel}^2} - \frac{(v_{\perp} - V)^2}{\theta_{\perp}^2} \right) d^3v, \quad (63)$$

$$= N_0 \left\{ \frac{1}{\sqrt{\pi} \theta_{\parallel}} \exp \left( -\frac{v_{\parallel}^2}{\theta_{\parallel}^2} \right) dv_{\parallel} \right\} \times \left\{ g_{\text{ring}}(v_{\perp}) dv_{\perp} \right\}, \quad (64)$$

$$g_{\text{ring}}(v_{\perp}) = \frac{2v_{\perp}}{\theta_{\perp}^2 C_2(\frac{V}{\theta_{\perp}})} \exp \left( -\frac{(v_{\perp} - V)^2}{\theta_{\perp}^2} \right), \quad (65)$$

$$C_2(x) = \exp(-x^2) + \sqrt{\pi}x \operatorname{erfc}(-x), \quad (66)$$

Here,  $V$  is the ring velocity,  $\theta_{\parallel}$  and  $\theta_{\perp}$  are parallel and perpendicular characteristic velocities, and  $\operatorname{erfc}(x)$  is the complementary error function. The perpendicular and parallel components are independent. The parallel component is assumed to be a Maxwellian. In the context of the solar wind,  $V$  corresponds to the solar-wind speed in the perpendicular direction. The pressures, the energy density, and the pressure anisotropy are given by [19]

$$P_{\perp} = \frac{N_0 m \theta_{\perp}^2}{4 C_2(\frac{V}{\theta_{\perp}})} \left\{ 2 \left( 1 + \frac{V^2}{\theta_{\perp}^2} \right) \exp \left( -\frac{V^2}{\theta_{\perp}^2} \right) + \sqrt{\pi} \frac{V}{\theta_{\perp}} \left( 3 + 2 \frac{V^2}{\theta_{\perp}^2} \right) \operatorname{erfc} \left( -\frac{V}{\theta_{\perp}} \right) \right\} \quad (67)$$

$$= \frac{N_0 m \theta_{\perp}^2}{2} \left\{ 1 + \frac{V^2}{\theta_{\perp}^2} + \frac{\sqrt{\pi}}{2 C_2(\frac{V}{\theta_{\perp}})} \frac{V}{\theta_{\perp}} \operatorname{erfc} \left( -\frac{V}{\theta_{\perp}} \right) \right\} \quad (68)$$

$$P_{\parallel} = \frac{1}{2} N_0 m \theta_{\parallel}^2, \quad \mathcal{E} = \frac{1}{4} N_0 m \left\{ \theta_{\parallel}^2 + 2 \theta_{\perp}^2 \left[ 1 + \frac{V^2}{\theta_{\perp}^2} + \frac{\sqrt{\pi}}{2 C_2(\frac{V}{\theta_{\perp}})} \frac{V}{\theta_{\perp}} \operatorname{erfc} \left( -\frac{V}{\theta_{\perp}} \right) \right] \right\} \quad (69)$$

$$A = \frac{\theta_{\perp}^2}{\theta_{\parallel}^2} \left\{ 1 + \frac{V^2}{\theta_{\perp}^2} + \frac{\sqrt{\pi}}{2 C_2(\frac{V}{\theta_{\perp}})} \frac{V}{\theta_{\perp}} \operatorname{erfc} \left( -\frac{V}{\theta_{\perp}} \right) \right\} - 1. \quad (70)$$

We also discuss the shell distribution with a Gaussian width [e.g., 13, 21, 25, 52]. We show the phase space density  $f_{\text{shell}}(\mathbf{v})$ , its radial form  $g_{\text{shell}}(v)$ , and an auxiliary function  $C_3(x)$ .

$$f_{\text{shell}}(\mathbf{v})d^3v = \frac{N_0}{2\pi\theta^3 C_3(\frac{V}{\theta})} \exp \left( -\frac{(|v| - V)^2}{\theta^2} \right) d^3v = N_0 \left\{ g_{\text{shell}}(v) dv \right\}, \quad (71)$$

$$g_{\text{shell}}(v) = \frac{2v^2}{\theta^3 C_3(\frac{V}{\theta})} \exp \left( -\frac{(|v| - V)^2}{\theta^2} \right), \quad (72)$$

$$C_3(x) = x \exp(-x^2) + \sqrt{\pi} \left( x^2 + \frac{1}{2} \right) \operatorname{erfc}(-x). \quad (73)$$

where  $V$  is the shell velocity and  $\theta$  is the characteristic velocity. We only consider the isotropic case. The pressure and the energy density are given by

$$P = \frac{N_0 m \theta^2}{12 C_3(\frac{V}{\theta})} \left\{ 2 \left( 5 + 2 \frac{V^2}{\theta^2} \right) \frac{V}{\theta} \exp \left( -\frac{V^2}{\theta^2} \right) + \sqrt{\pi} \left( 3 + 12 \frac{V^2}{\theta^2} + 4 \frac{V^4}{\theta^4} \right) \operatorname{erfc} \left( -\frac{V}{\theta} \right) \right\} \quad (74)$$

$$= \frac{N_0 m \theta^2}{6} \left\{ 5 + 2 \frac{V^2}{\theta^2} - \frac{\sqrt{\pi}}{C_3(\frac{V}{\theta})} \operatorname{erfc} \left( -\frac{V}{\theta} \right) \right\} \quad (75)$$

$$\mathcal{E} = \frac{N_0 m \theta^2}{4} \left\{ 5 + 2 \frac{V^2}{\theta^2} - \frac{\sqrt{\pi}}{C_3(\frac{V}{\theta})} \operatorname{erfc} \left( -\frac{V}{\theta} \right) \right\} \quad (76)$$

TABLE IV. Algorithms for ring and shell distributions. For the inverse transform method, please see the text. For the piecewise rejection method, see Appendix A and the procedure in Table. VII.

<b>Algorithm 6.1: ring distribution</b>
generate $U_1, U_2 \sim U(0, 1)$
generate $N \sim \mathcal{N}(0, 1)$
$R \leftarrow \text{CDF}_{\text{ring}}^{-1}(U_1)$ or PiecewiseRejection()
$v_{\perp 1} \leftarrow \theta_{\perp} R \cos(2\pi U_2)$
$v_{\perp 2} \leftarrow \theta_{\perp} R \sin(2\pi U_2)$
$v_{\parallel} \leftarrow \theta_{\parallel} N / \sqrt{2}$
<b>return</b> $v_{\perp 1}, v_{\perp 2}, v_{\parallel}$
<b>Algorithm 6.2: shell distribution</b>
generate $U_1, U_2, U_3 \sim U(0, 1)$
$R \leftarrow \text{CDF}_{\text{shell}}^{-1}(U_1)$ or PiecewiseRejection()
$v_x \leftarrow R(2U_2 - 1)$
$v_y \leftarrow 2R\sqrt{U_2(1 - U_2)} \cos(2\pi U_3)$
$v_z \leftarrow 2R\sqrt{U_2(1 - U_2)} \sin(2\pi U_3)$
<b>return</b> $v_x, v_y, v_z$

When  $V = 0$ , the distribution reverts to an isotropic Maxwellian. As we can imagine, both ring and shell distributions are artificially truncated at  $v_{\perp} = 0$  or at  $v = 0$ . This won't be a big issue for  $\theta \lesssim V$ , but becomes problematic for  $V \lesssim \theta$ .

To draw the ring and shell distributions in PIC simulation, perhaps the inverse transform method is used, even though it is not well documented. It is trivial to generate the parallel component of the ring distribution. *Umeda et al.* [44] inverted the perpendicular velocity from the CDF of the perpendicular distribution (Eq. (65)). This can be implemented by using a numerical table and a uniform variate  $U \sim U(0, 1)$ .

$$\text{CDF}_{\text{ring}}(v_{\perp}) = 1 - \frac{\exp\left(-\frac{(v_{\perp}-V)^2}{\theta_{\perp}^2}\right) + \sqrt{\pi} \frac{V}{\theta_{\perp}} \text{erfc}\left(\frac{v_{\perp}-V}{\theta_{\perp}}\right)}{C_2\left(\frac{V}{\theta}\right)} \quad (77)$$

$$v_{\perp} = \text{CDF}_{\text{ring}}^{-1}(U) \quad (78)$$

For the shell distribution, one can similarly construct the inverse transform method.

$$\text{CDF}_{\text{shell}}(v) = 1 - \frac{\frac{(v+V)}{\theta} \exp\left(-\frac{(v-V)^2}{\theta^2}\right) + \sqrt{\pi} \left(\frac{V^2}{\theta^2} + \frac{1}{2}\right) \text{erfc}\left(\frac{v-V}{\theta}\right)}{C_3\left(\frac{V}{\theta}\right)} \quad (79)$$

$$v = \text{CDF}_{\text{shell}}^{-1}(U) \quad (80)$$

Instead of the inverse transform, one can also use a piecewise rejection method for log-concave distributions [9], as described in Appendix A. Aside from detail implementation of the inverse transform, the procedures for the ring and shell distributions are listed in Algorithms 6.1 and 6.2 in Table IV.

Figures 4(a) and (b) shows perpendicular and radial particle distributions for  $V = 5\theta_{\perp}$  or  $V = 5\theta$ , together with numerical results. The blue histograms show Monre-Carlo results with  $10^6$  particles. They agree with the exact solutions (Eqs. (65) and (72)), indicated by the black lines, very well.

## VII. RING AND SHELL MAXWELLIANS

We discuss another ring and shell-shaped distributions, based on the scattering of seed Maxwellians. By gyrating a seed Maxwellian population, *Usami & Horiuchi* [45] has proposed the following axisymmetric distribution,

$$f_{\text{rM}}(\mathbf{v}) d^3 v = \frac{N_0}{\pi^{3/2} \theta_{\parallel} \theta_{\perp}^2} \exp\left(-\frac{v_{\parallel}^2}{\theta_{\parallel}^2} - \frac{v_{\perp}^2 + V^2}{\theta_{\perp}^2}\right) I_0\left(\frac{2v_{\perp}V}{\theta_{\perp}^2}\right) d^3 v \quad (81)$$

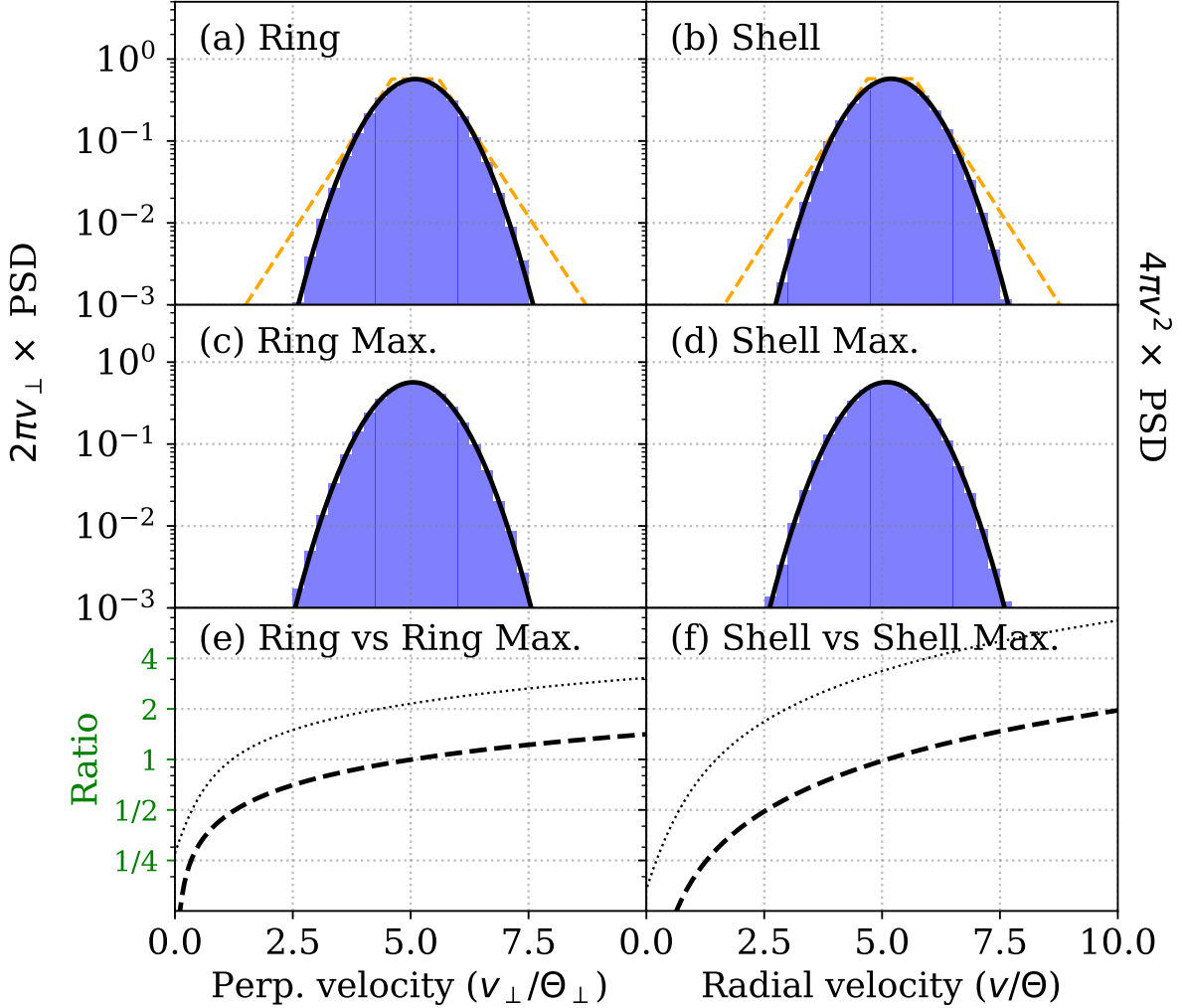


FIG. 4. Left) Perpendicular velocity distributions of the ring distributions,  $2\pi v_\perp \times g_{\text{ring}}(v_\perp)$ . Right) Radial velocity distributions of the shell distributions,  $4\pi v^2 \times f(v)$ . (a) The ring distribution (Eq. (63)), (b) the shell distribution (Eq. (71)), (c) the ring Maxwellian (Eq. (81)), and (d) the shell Maxwellian (Eq. (84)) are presented by the black lines. The blue histograms are numerical results with  $10^6$  particles. (e) The ratios of the ring distribution to the ring Maxwellian for  $V = 5\theta_\perp$  (dashed lines) and for  $V = \theta_\perp$  (dotted lines). (f) The ratios of the shell distribution to the shell Maxwellian for  $V = 5\theta$  (dashed lines) and for  $V = \theta$  (dotted lines). The orange dashed lines in Panels (a,b) are envelope functions for the piecewise rejection method, described in Appendix A.

where  $V$  is the ring velocity and  $I_0(x)$  is the zeroth-order modified Bessel function of the first kind. We call this distribution the ring Maxwell distribution or the ring Maxwellian<sup>1</sup>. Note that we employ a different convention for the characteristic velocity from the original paper, by a factor of  $\sqrt{2}$ . The phase space density is concave at  $v_\perp \simeq 0$  when  $V \leq \theta_\perp$ , while it has a ring-shaped structure when  $\theta_\perp < V$  [45]. The pressures, the energy density, and the

<sup>1</sup> The original authors call the distribution the ‘‘pseudo Maxwellian,’’ because they study near-Maxwellian cases,  $V \lesssim \theta_\perp$ . In this study, we call it the ring Maxwellian to emphasize its role as a ring-type distribution.

pressure anisotropy of the ring Maxwellian are as follows.

$$P_{\parallel} = \frac{1}{2} N_0 m \theta_{\parallel}^2, \quad P_{\perp} = \frac{1}{2} N_0 m (V^2 + \theta_{\perp}^2), \quad (82)$$

$$\mathcal{E} = \frac{1}{4} N_0 m (2V^2 + \theta_{\parallel}^2 + 2\theta_{\perp}^2), \quad A = \frac{V^2 + \theta_{\perp}^2}{\theta_{\parallel}^2} - 1. \quad (83)$$

In this study, we propose its shell-type extension, called the shell Maxwell distribution or the shell Maxwellian. As will be shown, the shell Maxwellian is spherically scattered from a seed Maxwellian, while the ring Maxwellian is axisymmetrically scattered. Its phase space density, pressure, and energy density are given by

$$f_{\text{sM}}(\mathbf{v}) d^3v = \frac{N_0}{4rV\theta(\pi)^{3/2}} \left\{ \exp\left(-\frac{(r-V)^2}{\theta^2}\right) - \exp\left(-\frac{(r+V)^2}{\theta^2}\right) \right\} d^3v, \quad (84)$$

$$P = N_0 m \left( \frac{1}{3} V^2 + \frac{1}{2} \theta^2 \right), \quad \mathcal{E} = \frac{1}{4} N_0 m (2V^2 + 3\theta^2). \quad (85)$$

where we use the radial speed  $r = |\mathbf{v}| = \sqrt{v_x^2 + v_y^2 + v_z^2}$  to emphasize its meaning in the polar coordinate system. When  $V \rightarrow 0$ , it recovers the Maxwell distribution

$$\lim_{V \rightarrow 0} f_{\text{sM}}(\mathbf{v}) = \frac{N_0}{2r\theta(\pi)^{3/2}} \lim_{V \rightarrow 0} \frac{e^{-\frac{(r-V)^2}{\theta^2}} - e^{-\frac{(r+V)^2}{\theta^2}}}{2V} = \frac{-N_0}{2r\theta(\pi)^{3/2}} \frac{d}{dx} e^{-x^2/\theta^2} \Big|_{x=r} = \frac{N_0}{(\pi\theta^2)^{3/2}} e^{-r^2/\theta^2} \quad (86)$$

When  $\theta = 0$ , the pressure and energy density recover those of a thin shell,

$$P = \frac{1}{3} N_0 m V^2, \quad \mathcal{E} = \frac{1}{2} N_0 m V^2. \quad (87)$$

Here we derive Eq. (84). We first place the seed Maxwellian, whose bulk velocity is  $\mathbf{V}$ .

$$f(\mathbf{v}) = \frac{N_0}{(\pi\theta^2)^{3/2}} \exp\left(-\frac{(\mathbf{v} - \mathbf{V})^2}{\theta^2}\right), \quad (88)$$

Then we scatter the pitch angle, such that the distribution is fully isotropized. Using the radial velocity  $r$ , the final state  $f_{\text{sM}}(r) 4\pi r^2 dr$  should satisfy the following relation, with help from polar coordinates of  $(r, \alpha, \varphi)$  and a pitch-angle cosine,  $\mu \equiv \cos \alpha$ .

$$f_{\text{sM}}(r) 4\pi r^2 dr = \frac{N_0}{(\pi\theta^2)^{3/2}} \left\{ \iint \exp\left(-\frac{r^2 + V^2}{\theta^2}\right) \exp\left(\frac{2rV \cos \alpha}{\theta^2}\right) \sin \alpha d\alpha d\varphi \right\} r^2 dr, \quad (89)$$

$$= \frac{2\pi N_0}{(\pi\theta^2)^{3/2}} \exp\left(-\frac{r^2 + V^2}{\theta^2}\right) \left\{ \int_{-1}^1 \exp\left(\frac{2rV\mu}{\theta^2}\right) d\mu \right\} r^2 dr, \quad (90)$$

This immediately gives Eq. (84). The energy distribution resembles that of a drifting Maxwellian, discussed by Karlický *et al.* [16, Section 2]. Maclaurin expansion of Eq. (84) gives further insights:

$$f_{\text{sM}}(r) = \frac{N_0}{4rV\theta(\pi)^{3/2}} \exp\left(-\frac{V^2}{\theta^2}\right) \exp\left(-\frac{r^2}{\theta^2}\right) \left\{ \exp\left(\frac{2rV}{\theta^2}\right) - \exp\left(-\frac{2rV}{\theta^2}\right) \right\} \quad (91)$$

$$\simeq \frac{N_0}{4rV\theta(\pi)^{3/2}} \exp\left(-\frac{V^2}{\theta^2}\right) \left(1 - \frac{r^2}{\theta^2} + \mathcal{O}(r^4)\right) \left\{ \frac{4rV}{\theta^2} \left(1 + \frac{2r^2V^2}{3\theta^4} + \mathcal{O}(r^4)\right) \right\} \quad (92)$$

$$\simeq \frac{N_0}{(\pi\theta^2)^{3/2}} \exp\left(-\frac{V^2}{\theta^2}\right) \left\{ 1 + \left(\frac{2V^2 - 3\theta^2}{3\theta^4}\right) r^2 + \mathcal{O}(r^4) \right\} \quad (93)$$

This indicates that the shell Maxwellian has a peak at the center, and it no longer looks like a shell when  $V \leq \sqrt{3/2}\theta \simeq 1.22\theta$ . The phase space density has a shell-shaped structure when  $V > \sqrt{3/2}\theta$ .

Since they are scattered from the seed Maxwellian, the ring and shell Maxwellians can be easily generated in PIC simulation. One can generate a Maxwell distribution with a thermal velocity, and then rotate the particle velocity in an axisymmetric or spherical manner. The procedures are presented in Algorithms 7.1 and 7.2 in Table V. They are simpler than Algorithms 6.1 and 6.2 which require additional procedures. We have also carried out Monre-Carlo

TABLE V. Algorithms for the ring and shell Maxwellians

<b>Algorithm 7.1: ring Maxwellian</b>
generate $N_1, N_2, N_3 \sim \mathcal{N}(0, 1)$
generate $U \sim U(0, 1)$
$v_{\parallel} \leftarrow (\theta_{\parallel}/\sqrt{2})N_1$
$v_{\perp 1} \leftarrow (\theta_{\perp}/\sqrt{2})N_2 + V \cos(2\pi U)$
$v_{\perp 2} \leftarrow (\theta_{\perp}/\sqrt{2})N_3 + V \sin(2\pi U)$
<b>return</b> $v_{\parallel}, v_{\perp 1}, v_{\perp 2}$
<b>Algorithm 7.2: shell Maxwellian</b>
generate $N_1, N_2, N_3 \sim \mathcal{N}(0, 1)$
generate $U_1, U_2 \sim U(0, 1)$
$v_x \leftarrow (\theta/\sqrt{2})N_1 + V(2U_1 - 1)$
$v_y \leftarrow (\theta/\sqrt{2})N_2 + 2V\sqrt{U_1(1 - U_1)} \cos(2\pi U_2)$
$v_z \leftarrow (\theta/\sqrt{2})N_3 + 2V\sqrt{U_1(1 - U_1)} \sin(2\pi U_2)$
<b>return</b> $v_x, v_y, v_z$

tests for  $V = 5\theta_{\perp}$  or  $V = 5\theta$  with  $10^6$  particles. Figures 4(c) and (d) compare perpendicular and radial distributions of the distributions (black lines) and numerical results (blue histograms).

Figure 4(e) compares the ring distribution and the ring Maxwellian for  $V = 5\theta$  (solid line) and for  $V = \theta$  (dotted line), and Figure 4(f) compares the shell distributions in the same format.

$$\frac{f_{\text{ring}}(v_{\perp}) 2\pi v_{\perp}}{f_{\text{rM}}(v_{\perp}) 2\pi v_{\perp}} = \frac{1}{C_2(\frac{V}{\theta_{\perp}})} \frac{\exp\left(\frac{2v_{\perp}V}{\theta_{\perp}^2}\right)}{I_0\left(\frac{2v_{\perp}V}{\theta_{\perp}^2}\right)}, \quad \frac{f_{\text{shell}}(r) 4\pi r^2}{f_{\text{sM}}(r) 4\pi r^2} = \frac{2rV\sqrt{\pi}}{\theta^2 C_3(\frac{V}{\theta})} \left\{1 - \exp\left(-\frac{4rV}{\theta^2}\right)\right\}^{-1}, \quad (94)$$

As evident in Figure 4(e), the two ring distributions are very similar around the peaks for  $V = 5\theta_{\perp}$ . The phase space densities are maximum at  $v_{\perp} = 5\theta_{\perp}$  for the ring distribution, and at  $v_{\perp} \approx 4.95\theta_{\perp}$  for the ring Maxwellian. Also, in Figure 4(f), the two shell distributions are similar around the peaks for  $V = 5\theta$ . The maximums are located at  $v = 5\theta$  for the shell distribution, and at  $v \approx 4.9\theta$  for the shell Maxwellian. These results suggest that the ring and shell Maxwellians are good alternatives for the ring and shell distributions with Gaussian width. On the other hand, when  $V \lesssim \theta$ , the ring (shell) distribution and the ring (shell) Maxwellian are very different, as shown by the dotted lines. As already stated, the artificial boundary of the ring and shell distributions becomes problematic.

## VIII. OTHER ISOTROPIC DISTRIBUTIONS

We present numerical procedures for two isotropic distributions. First, we discuss the super-Gaussian distribution, also known as the self-similar distribution or the multivariate exponential power distribution. The distribution has long been discussed in laser plasmas [11, 28] but also useful in space plasmas [48]. It is given by

$$f_{\text{sg}}(\mathbf{v}) d^3 v = \frac{N_0 p}{4\pi\theta^3 \Gamma(3/p)} \exp\left\{-\left(\frac{v}{\theta}\right)^p\right\} d^3 v, \quad (95)$$

where  $\theta$  is the characteristic velocity and  $p$  is the index. The pressure and energy density are:

$$P = \frac{1}{3} N_0 m \theta^2 \frac{\Gamma(5/p)}{\Gamma(3/p)}, \quad \mathcal{E} = \frac{1}{2} N_0 m \theta^2 \frac{\Gamma(5/p)}{\Gamma(3/p)}, \quad (96)$$

We consider the radial distribution,

$$F_{\text{sg}}(v) dv = f_{\text{sg}}(v) 4\pi v^2 dv = \frac{N_0 p}{\theta^3 \Gamma(3/p)} \exp\left\{-\left(\frac{v}{\theta}\right)^p\right\} v^2 dv, \quad (97)$$

Using an auxiliary variable  $x \equiv (v/\theta)^p$ , we find that it follows a gamma distribution,

$$F_{\text{sg}}(x) dx = N_0 \left\{ \text{Ga}(x; 3/p, 1) dx \right\}, \quad (98)$$

TABLE VI. Algorithms for super-Gaussian and filled-shell distributions.

<b>Algorithm 8.1: super Gaussian</b>
generate $X \sim \text{Ga}(3/p, 1)$
generate $U_1, U_2 \sim U(0, 1)$
$v \leftarrow \theta X^{1/p}$
$v_x \leftarrow v (2U_1 - 1)$
$v_y \leftarrow 2v \sqrt{U_1(1 - U_1)} \cos(2\pi U_2)$
$v_z \leftarrow 2v \sqrt{U_1(1 - U_1)} \sin(2\pi U_2)$
<b>return</b> $v_x, v_y, v_z$

<b>Algorithm 8.2: filled-shell distribution</b>
generate $U_1, U_2, U_3 \sim U(0, 1)$
$v \leftarrow V \cdot (U_1)^{1/(3+p)}$
$v_x \leftarrow v (2U_2 - 1)$
$v_y \leftarrow 2v \sqrt{U_2(1 - U_2)} \cos(2\pi U_3)$
$v_z \leftarrow 2v \sqrt{U_2(1 - U_2)} \sin(2\pi U_3)$
<b>return</b> $v_x, v_y, v_z$

Thus, the velocity  $v$  can be drawn from a gamma variate  $X_{\text{Ga}(3/p, 1)}$ ,

$$v = \theta \left( X_{\text{Ga}(3/p, 1)} \right)^{1/p} \quad (99)$$

Then one can obtain  $\mathbf{v}$  by scattering the vector in three dimensions. The procedure is shown in Algorithm 8.1 (Table VI).

Finally we consider the filled-shell distribution, which plays a role in a distant heliosphere. The phase space density follows a power-law  $\propto v^p$  inside a spherical shell ( $v \leq V$ ),

$$f_{\text{fs}}(\mathbf{v}) = \frac{N_0(3+p)}{4\pi V^{3+p}} v^p \cdot \mathcal{H}(V - v) \quad (100)$$

Here,  $\mathcal{H}(x)$  is the Heaviside step function and  $p$  is the spectral index ( $p > -3$ ). The pressure and energy density are given by

$$P = \frac{3+p}{3(5+p)} N_0 m V^2, \quad \mathcal{E} = \frac{3+p}{2(5+p)} N_0 m V^2. \quad (101)$$

The spectral index varies from problem to problem. The so-called Vasyliunas–Siscoe model [47] employs  $p = -3/2$  [e.g., 55], but we find other choices in the literature [e.g.,  $p = 1$ ; 14].

Since  $f_{\text{fs}}(v)4\pi v^2 \propto v^{2+p}$ , one can generate the velocity  $v = V \cdot (U_1)^{1/(3+p)}$ , using a uniform variate  $U_1 \sim U(0, 1)$ . A full procedure is presented in Algorithm 8.2 (Table VI).

The two procedures are numerically tested, by using  $10^6$  particles. We set  $p = 3$  and  $\theta = 1$  for the super Gaussian, and  $p = -3/2$  and  $V = 2$  for the filled-shell distribution. Their Monte Carlo results are shown in the two panels in Figure 5. The exact solutions and numerical results are in excellent agreement.

## IX. NUMERICAL TEST

Our algorithms are tested in each sections (Sections III–VIII), either in 1-D histograms and in the 2-D colormaps, but we present one more test to verify them. We have conducted a Kullback–Leibler (KL) divergence test to our datasets, as done in our earlier study [57]. For the  $i$ -th bin in 1-D histograms or the  $i$ -th cell in 2-D colormaps, we compare exact densities  $P(i)$  and normalized particle count numbers  $Q(i)$ . Similarity between  $P$  and  $Q$  is evaluated by the KL divergence, also known as the cross entropy,

$$D_{\text{KL}}(P\|Q) \equiv \sum_i (P(i) + \epsilon) \log \frac{P(i) + \epsilon}{Q(i) + \epsilon} \quad (102)$$

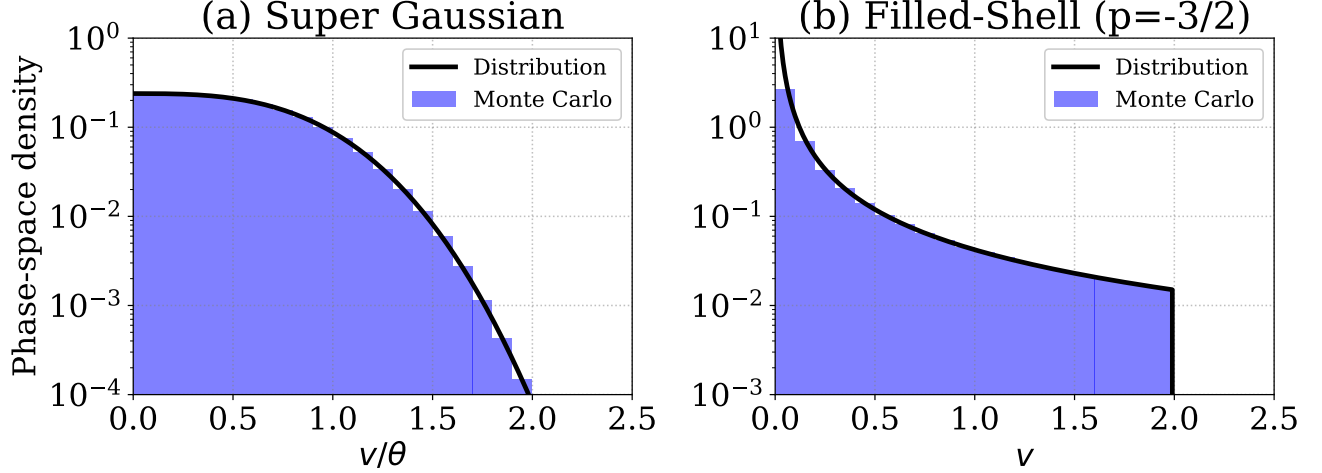


FIG. 5. The phase space densities (black lines) and Monte Carlo results of  $10^6$  particles (blue histograms) for (a) the super Gaussian distribution ( $p = 3, \theta = 1$ ) and (b) the filled-shell distribution ( $p = -3/2, V = 2$ ) are presented.

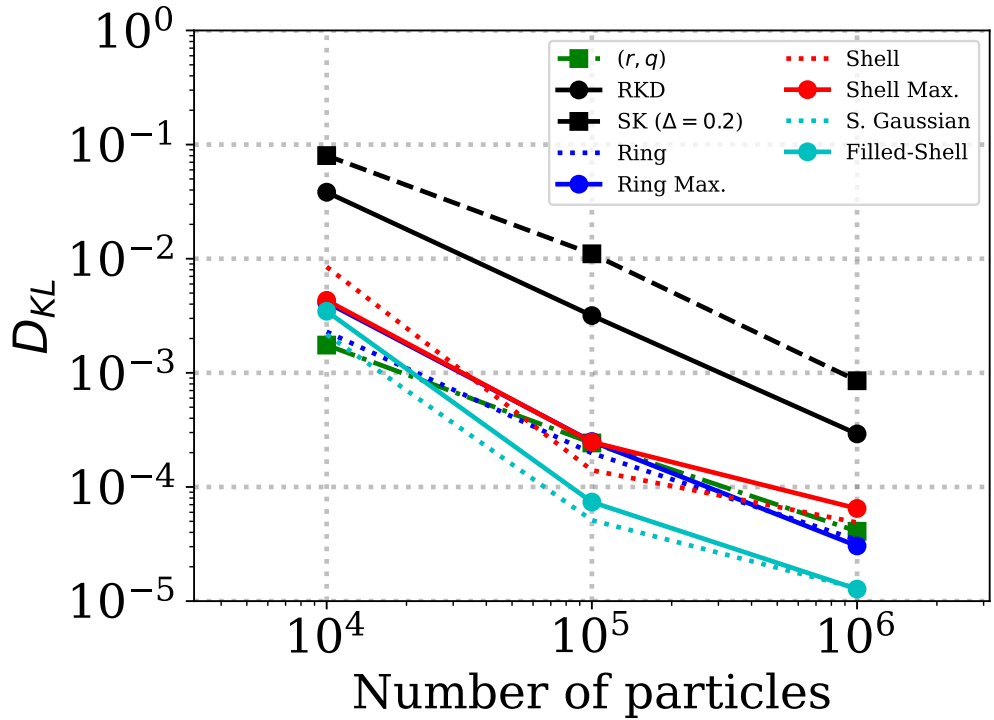


FIG. 6. The Kullback–Leibler divergence of the numerical distributions from the analytical solutions (Eq. (102)).

where a small number  $\epsilon = 10^{-10}$  is added to avoid zero. It is non-negative, and it becomes zero when and only when the two distributions are identical.

Fig. 6 shows the KL divergence for the nine distributions, as a function of the total particle number. The parameters are detailed in the relevant sections. For the subtracted Kappa distribution,  $\Delta = 0.2$  is set (Fig. 3(b)). For the ring and shell distributions (Figs. 4(a,b)), the piecewise rejection method is used. Note that it is not meaningful to compare different distributions quantitatively, because the data come from sources of difference sizes: PSDs, omni-directional

velocity distributions ( $4\pi v^2 f(v)$ ), or a 2-D colormap. Importantly,  $D_{KL}$  approaches zero in all the cases, as we increase the particle number. This suggests that the Monte Carlo results approximate the exact distributions very well.

## X. DISCUSSION AND SUMMARY

In our earlier papers [56, 57], we have proposed numerical procedures using three elemental variates: the uniform variate, the normal variate, and the gamma variate. In this paper, we have successfully extended this approach to nine different VDFs: the  $(r, q)$  distribution, the regularized Kappa distribution, the subtracted Kappa distribution, the ring distribution, the shell distribution, the ring Maxwellian, the shell Maxwellian, the super-Gaussian, and the filled-shell distributions. With help from the basic statistical distributions (Section II), mathematics behind the recipes are fully explained. The numerical recipes for all the VDFs are provided in Tables, making it easy for users to implement them in the code. The algorithms are tested in each sections, as well as in Section IX.

In Section III, we have discussed the  $(r, q)$  distribution that generalizes the Kappa and flattop distributions. One can use either of the beta-prime method and the piecewise rejection method, if one is aware of limitations of each. Sections IV and V have discussed the two advanced Kappa distributions. For the regularized Kappa distribution, the two rejection methods and their preferred parameter spaces are described. The simple procedure was proposed for a very recent model of the subtracted Kappa distribution. The loss-cone filling parameter  $\Delta$  is considered in Eq. (62). A previous procedure for the subtracted Maxwellian [57, Section 2] can be similarly modified to incorporate the filling parameter. In addition, after submitting this paper, *Min et al.* [26] independently developed the same procedure for their PIC simulation (see Appendix in their paper). This work provides a more detailed explanation to this cutting-edge method.

In Section VII, we have introduced the ring Maxwellian and the shell Maxwellian. We would propose them as alternatives for the ring and shell distributions in Section VI. When the ring/shell velocity substantially exceeds the thermal width,  $V \gg \theta$ , these distributions are similar to the conventional ring and shell distributions. If we evaluate their differences using Eq. (94) at  $V \pm \sigma$ , where  $\sigma = \theta/\sqrt{2}$  is the standard deviation, the two ring distributions are in agreement within 10% for  $V \gtrsim 3.9\theta_{\perp}$ , and the two shell distributions are in agreement within 15% for  $V \gtrsim 5.25\theta$ . Physically, the new Maxwellians correspond to the radial or spherical scattering of a seed population, whereas the ring and shell distributions lack a justification for their Gaussian width. When  $V \lesssim \theta$ , the conventional distributions become somewhat artificial near  $v = 0$ , and probably it does not make sense to employ them. In contrast, the (ring and shell) Maxwellians have no artificial problem at  $v = 0$ , but they are no longer ring- or shell-shaped when  $V \leq \theta_{\perp}$  (ring) or  $\leq \sqrt{3/2}\theta$ . Practically, the new Maxwellians are easier to use. As shown in Sections VI and VII, it is much easier to estimate pressures, pressure anisotropies, and energy density for the new Maxwellians than those for the conventional distributions. Also, Monte Carlo procedures for the new Maxwellians are much simpler than those for the conventional distributions, as shown in Tables IV and V. These facts suggest that the ring or shell Maxwellians are favorable for modeling of heliospheric kinetic processes in ring or shell-shaped VDFs.

Technically, the proposed algorithms raise minor concerns when deployed on graphics processing units (GPUs). In particular, algorithms that rely on the rejection method can be inefficient on GPUs. This is because the number of iterations required by the rejection loop may vary from thread to thread, which is not well suited to the GPU's execution model. Furthermore, at the time of writing, neither NVIDIA's `cuRAND` library nor AMD's `hipRAND` library provides gamma generators, although both libraries support uniform and normal variates. Consequently, we need to generate gamma variates on the CPU or to implement custom gamma generators on the GPU. Since GPU computation has only recently become popular in heliophysics, further investigation is needed to see whether these issues are critical and to find other potential problems.

Together with our earlier works [56, 57], we can now generate a wide variety of single-component VDFs in heliophysics for particle simulations. In more complex scenarios, VDFs may have multiple components, some of which are not approximated by well-known VDFs. For example, solar-wind electrons often consists of core, halo, and strahl populations. In such cases, it may be necessary not only to develop separate procedures for each component, but also to use a fully numerical inversion method [4]. This should be evaluated on a case-by-case basis.

In summary, we have provided numerical procedures for generating nine different VDFs in heliophysics research. We hope that this work will make kinetic modeling of heliospheric plasma processes easier than before.

## ACKNOWLEDGEMENTS

SU was supported by Grant-in-Aid for Scientific Research (C) 22K03581 from the Japan Society for the Promotion of Science (JSPS). SM was supported by Grant-in-Aid for Scientific Research (B) 23K22558 from JSPS.

## AUTHOR DECLARATIONS

### Conflict of Interest

The authors have no conflicts to disclose.

### Author Contributions

**SZ:** Conceptualization (lead), Formal analysis (lead), Investigation (equal), Methodology (lead), Visualization (lead), Writing – original draft (lead), Writing – review & editing (equal), **SU:** Conceptualization (supporting), Investigation (equal), Writing – review & editing (equal), **SM:** Conceptualization (supporting), Investigation (equal), Writing – review & editing (equal)

### Data Availability Statement

The Jupyter notebook for this article is archived in Zenodo [61].

## Appendix A: Piecewise rejection method for log-concave distributions

We first rewrite the target distributions.

$$g(v) = \begin{cases} g_{\text{ring}}(v_{\perp}) & (\text{Eq. (65); ring distribution}) \\ g_{\text{shell}}(v) & (\text{Eq. (72); shell distribution}) \end{cases} \quad (\text{A1})$$

The distribution has a maximum at the most probable speed:

$$v_m = \begin{cases} \frac{1}{2} \left( V + \sqrt{V^2 + 2\theta_{\perp}^2} \right) & (\text{ring}) \\ \frac{1}{2} \left( V + \sqrt{V^2 + 4\theta^2} \right) & (\text{shell}) \end{cases} \quad (\text{A2})$$

With this in mind, we define left and right contact points,

$$v_L \equiv v_m - \theta, \quad v_R \equiv v_m + \theta \quad (\text{A3})$$

To ensure  $v_L > 0$ ,  $V > \theta/2$  ( $V > 0$ ) is required in the case of the ring (shell) distribution. This is reasonable limitation, because we usually consider  $V \gtrsim \theta$ .

Since  $g(x)$  is log-concave, i.e.,  $(\log g_{\text{ring}}(v_{\perp}))'' \propto -(1/v_{\perp}^2 + 2/\theta_{\perp}^2) < 0$  and  $(\log g_{\text{shell}}(v))'' \propto -(2/v^2 + 2/\theta^2) < 0$ , we can define exponential envelope functions that touch the distribution at  $v = v_L, v_m$ , and  $v_R$ .

$$G(p) = \begin{cases} g(v_L) \exp \left( \frac{v - v_L}{\lambda(v_L)} \right) & (0 \leq v < x_L) \\ g(v_m) & (x_L \leq v < x_R) \\ g(v_R) \exp \left( -\frac{v - v_R}{\lambda(v_R)} \right) & (x_R \leq v < \infty) \end{cases} \quad (\text{A4})$$

Here,  $\lambda(v) = |g(v)/g'(v)|$  is the length scale and

$$x_L = v_L - \lambda(v_L) \log \frac{g(v_L)}{g(v_m)}, \quad x_R = v_R + \lambda(v_R) \log \frac{g(v_R)}{g(v_m)} \quad (\text{A5})$$

are the two switching points. As an example, the envelope functions are drawn by the dashed orange lines in Figures 4(a,b). The ratio of the areas below the envelopes is  $\lambda(v_L) : (x_R - x_L) : \lambda(v_R)$ . Then a rejection algorithm can be constructed, as shown in Table VII. The acceptance efficiency is

$$\text{eff} = \frac{1}{g(v_m) \{ (x_R - x_L) + \lambda(v_R) + \lambda(v_L) \}}. \quad (\text{A6})$$

TABLE VII. Piecewise rejection method

<b>Piecewise rejection method for Algorithms 6.1 and 6.2</b>	
$V > \theta_{\perp}/2$ is required for the ring distribution	
$g(v)$ is defined by Eq. (A1) (Eq. (65) or (72))	
$v_m$ is defined by Eq. (A2)	
$g_{max} \leftarrow g(v_m)$ $v_L \leftarrow v_m - \theta, \quad \lambda_L \leftarrow \frac{g(v_L)}{g'(v_L)}, \quad x_L \leftarrow v_L - \lambda_L \log \frac{g(v_L)}{g_{max}}$ $v_R \leftarrow v_m + \theta, \quad \lambda_R \leftarrow \left  \frac{g(v_R)}{g'(v_R)} \right , \quad x_R \leftarrow v_R + \lambda_R \log \frac{g(v_R)}{g_{max}}$ $S \leftarrow \lambda_L + (x_R - x_L) + \lambda_R,$ $p_L \leftarrow \frac{\lambda_L}{S}, \quad p_R \leftarrow \frac{\lambda_R}{S}, \quad p_C \leftarrow 1 - p_L - p_R$ <b>repeat</b>	
$\text{generate } U_1, U_2 \sim U(0, 1)$ <b>if</b> $U_1 \leq p_C$ <b>then</b> $v \leftarrow x_L + (x_R - x_L)(U_1/p_C)$ <b>if</b> $U_2 < g(v)/g_{max}$ <b>break</b> <b>else if</b> $U_1 \leq p_C + p_L$ <b>then</b> $u \leftarrow (U_1 - p_C)/p_L$ $v \leftarrow x_L + \lambda_L \log u$ <b>if</b> $0 < v$ <b>and</b> $uU_2 < g(v)/g_{max}$ <b>break</b> <b>else</b> $u \leftarrow (U_1 - p_C - p_L)/p_R$ $v \leftarrow x_R - \lambda_R \log u$ <b>if</b> $uU_2 < g(v)/g_{max}$ <b>break</b> <b>endif</b> <b>end repeat</b> <b>return</b> $v$	

This gives  $\gtrsim 86\%$  for  $V \gtrsim \theta$  and  $88\%-89\%$  for  $V \gtrsim 2\theta$  for both ring and shell distributions. In practice, the normalization constant in  $g(x)$  can be dropped in the procedure (Table VII).

---

[1] Abdul R. F., & R. L. Mace (2014), A method to generate kappa distributed random deviates for particle-in-cell simulations, *Comput. Phys. Commun.*, *185*, 2383–2386, doi:10.1016/j.cpc.2014.05.006.

[2] Abdul R. F., & R. L. Mace (2015), One-dimensional particle-in-cell simulations of electrostatic Bernstein waves in plasmas with kappa velocity distributions, *Phys. Plasmas*, *22*, 102107, doi:10.1063/1.4933005.

[3] Ahrens, J. H., & U. Dieter (1974), Computer Methods for Sampling from Gamma, Beta, Poisson and Binomial Distributions, *Computing*, *12*, 223–246, doi:10.1007/BF02293108.

[4] An, X., A. Artemyev, V. Angelopoulos, S. Lu, P. Pritchett, V. Decyk (2022), Fast inverse transform sampling of non-Gaussian distribution functions in space plasmas. *J. Geophys. Res.*, *127*, e2021JA030031, doi:10.1029/2021JA030031.

[5] Ashour-Abdalla, M., & C. F. Kennel (1978), Nonconvective and convective electron cyclotron harmonic instabilities, *J. Geophys. Res.*, *83*, 1531–1543, doi:10.1029/JA083iA04p01531.

[6] Best, D. J. (1983), A Note on Gamma Variate Generators with Shape Parameter less than Unity, *Computing*, *30*, 185–188, doi:10.1007/BF02280789.

[7] Birdsall, C. K., & A. B. Langdon (1985), *Plasma Physics via Computer Simulation*, McGraw-Hill, New York.

[8] Box G. E. P., & M. E. Muller (1958), A note on the generation of random normal deviates, *Ann. Math. Stat.*, *29*, 610–611, doi:10.1214/aoms/1177706645.

[9] Devroye, L. (1986), *Non-Uniform Random Variate Generation*, Springer-Verlag, available at <http://luc.devroye.org/rnbookindex.html>.

[10] Dory, R. A., G. E. Guest, & E. G. Harris (1965), Unstable Electrostatic Plasma Waves Propagating Perpendicular to a Magnetic Field, *Phys. Rev. Lett.*, *14*, 131–133, doi:10.1103/PhysRevLett.14.131.

[11] Dum, C. T., R. Chodura, & D. Biskamp (1974), Turbulent Heating and Quenching of the Ion Sound Instability, *Phys.*

*Rev. Lett.*, **32**, 1231, doi:10.1103/PhysRevLett.32.1231.

[12] Feldman, W. C., S. J. Bame, S. P. Gary, J. T. Gosling, D. McComas, & M. F. Thomsen (1982), Electron Heating Within the Earth's Bow Shock, *Phys. Rev. Lett.*, **49**, 199–201, doi:10.1103/PhysRevLett.49.199.

[13] Freund, H. P., & C. S. Wu (1988), Stability of a spherical shell distribution of pickup ions, *J. Geophys. Res.*, **93**, 14277–14283, doi:10.1029/JA093iA12p14277.

[14] Giacalone, J., M. Kornbleuth, M. Opher, M. Gkioulidou, J. Køta, E. Puzzoni, J. D. Richardson, & G. P. Zank (2025), Hybrid Simulations of Interstellar Pickup Ions at the Solar Wind Termination Shock Revisited, *Astrophys. J.*, **980**, 29, doi:10.3847/1538-4357/ada89c.

[15] Hockney, R. W., & J. W. Eastwood (1981), *Computer simulation using particles*, McGraw-Hill, New York.

[16] Karlický, M., E. Dzifčáková, & J. Dudík (2012), On the physical meaning of  $n$ -distributions in solar flares, *Astron. Astrophys.*, **537**, A36, doi:10.1051/0004-6361/201117860.

[17] Kennel, C. F. (1966), Low-Frequency Whistler Mode, *Phys. Fluids*, **9**, 2190–2202, doi:10.1063/1.1761588.

[18] Kroese, D. P., T. Taimre, & Z. I. Botev (2011), *Handbook of Monte Carlo methods*, John Wiley & Sons.

[19] Kumar, S., S. K. Dixit, & A. K. Gwal (1997), Electron cyclotron waves in the presence of parallel electric fields in the Earth's auroral plasma, *Ann. Geophys.*, **15**, 24–28, doi:10.1007/s00585-997-0024-3.

[20] Lazar, M., & Fichtner, H. (eds.) (2021), *Kappa Distributions; From Observational Evidences via Controversial Predictions to a Consistent Theory of Nonequilibrium Plasmas*, Astrophysics and Space Science Library, vol. 464, Berlin: Springer, ISBN: 978-3-030-82623-9.

[21] Liu, K., S. P. Gary, & D. Winske (2011), Excitation of magnetosonic waves in the terrestrial magnetosphere: Particle-in-cell simulations, *J. Geophys. Res.*, **116**, A07212, doi:10.1029/2010JA016372.

[22] Livadiotis, G. (ed.) (2017), *Kappa Distributions: Theory and Applications in Plasmas*, Elsevier, Amsterdam.

[23] Marsaglia G., & W. W. Tsang (2000), A simple method for generating gamma variables, *ACM Trans. Math. Software*, **26**, 363–372, doi:10.1145/358407.358414.

[24] Matsukiyo, S., & M. Scholer (2014), Simulations of pickup ion mediated quasiperpendicular shocks: Implications for the heliospheric termination shock, *J. Geophys. Res.*, **119**, 2388–2399, doi:10.1002/2013JA019654.

[25] Min, K., & K. Liu (2015), Fast magnetosonic waves driven by shell velocity distributions, *J. Geophys. Res.*, **120**, 2739–2753, doi:10.1002/2015JA021041.

[26] Min, K., Miyoshi, Y., & K. Liu (2025), Linear analysis and PIC simulations of electron cyclotron harmonic instability driven by a subtracted-kappa velocity distribution, *Phys. Plasmas*, **32**, 122901, doi:10.1063/5.0305058.

[27] Möbius, E., D. Hovestadt, B. Klecker, M. Scholer, G. Gloeckler, & F. M. Ipavich (1985), Direct observation of  $\text{He}^+$  pick-up ions of interstellar origin in the solar wind, *Nature* **318**, 426–429, doi:10.1038/318426a0.

[28] Mora, P., & H. Yahi (1982), Thermal heat-flux reduction in laser-produced plasmas, *Phys. Rev. A*, **26**, 2259, doi:10.1103/PhysRevA.26.2259.

[29] Nakanotani M., G. P. Zank, & L.-L. Zhao (2023), Pickup Ion-Mediated Magnetic Reconnection in the Outer Heliosphere, *Astrophys. J.*, **949**, L2, doi:10.3847/2041-8213/acd33f.

[30] Oka, M., T. D. Phan, M. Øieroset, D. L. Turner, J. F. Drake, X. Li, S. A. Fuselier, D. J. Gershman, B. L. Giles, R. E. Ergun, R. B. Torbert, H. Y. Wei, R. J. Strangeway, C. T. Russell, & J. L. Burch (2022), Electron energization and thermal to non-thermal energy partition during earth's magnetotail reconnection, *Phys. Plasmas*, **29**, 052904, doi:10.1063/5.0085647.

[31] Olbert, S. (1968), Summary of Experimental Results from M.I.T. Detector on IMP-1. In: Carovillano, R. L., McClay, J. F., Radoski, H. R. (Eds.) *Physics of the Magnetosphere* (pp. 641–659). Astrophysics and Space Science Library, vol. 10, Springer, Dordrecht, doi:10.1007/978-94-010-3467-8\_23.

[32] Olver, F. W. J., A. B. Olde Daalhuis, D. W. Lozier, B. I. Schneider, R. F. Boisvert, C. W. Clark, B. R. Miller, B. V. Saunders, H. S. Cohl, and M. A. McClain. 2025, *NIST Digital Library of Mathematical Functions*, <https://dlmf.nist.gov/> (DLMF), Release 1.2.4 of 2025-03-15.

[33] Pyakurel, P. S., M. Swisdak, S. Eriksson, B. L. Shrestha, Y.-H. Liu, J. M. TenBarge, M. A. Shay, and T. D. Phan (2025), Kinetic Simulation of Magnetic Reconnection with Pickup Ions: Shell Stability and Reconnection Rate Analysis, *Astrophys. J.*, **988**, 119, doi:10.3847/1538-4357/ade3db.

[34] Qureshi, M. N. S., W. Nasir, W. Masood, P. H. Yoon, H. A. Shah, & S. J. Schwartz (2014), Terrestrial ion roars and non-Maxwellian distribution, *J. Geophys. Res.*, **119**, 10,059–10,067, doi:10.1002/2014JA020476.

[35] Qureshi, M. N. S., W. Nasir, R. Bruno, & W. Masood (2019), Whistler instability based on observed flat-top two-component electron distributions in the Earth's magnetosphere, *Mon. Notices Royal Astron. Soc.*, **488**, 954–964, doi:10.1093/mnras/stz1702.

[36] Qureshi, M. N. S., H. A. Shah, G. Murtaza, S. J. Schwartz, & F. Mahmood (2004), Parallel propagating electromagnetic modes with the generalized  $(r,q)$  distribution function, *Phys. Plasmas*, **11**, 3819, doi:10.1063/1.1688329.

[37] Richard, L., Y. Khotyaintsev, C. Norgren, K. Steinvall, D. Graham, J. Egedal, A. Vaivads, & R. Nakamura (2025). Electron Heating by Parallel Electric Fields in Magnetotail Reconnection, *Phys. Rev. Lett.*, **134**, 215201, doi:10.1103/PhysRevLett.134.215201.

[38] Scherer, K., H. Fichtner, & M. Lazar (2017), Regularized  $\kappa$ -distributions with non-diverging moments, *Europhys. Lett.*, **120**, 50002, doi:10.1209/0295-5075/120/50002.

[39] Scherer, K., E. Husidic, M. Lazar, & H. Fichtner (2020), The  $\kappa$ -cookbook: a novel generalizing approach to unify  $\kappa$ -like distributions for plasma particle modelling, *Mon. Notices Royal Astron. Soc.*, **497**, 1738–1756, doi:10.1093/mnras/staa1969.

[40] Summers, D., & S. Stone (2025), The subtracted-kappa distribution and its properties, *Phys. Plasmas*, **32**, 012112, doi:10.1063/5.0239741.

[41] Summers, D., & R. M. Thorne (1991), The modified plasma dispersion function, *Phys. Fluids B*, **3**, 1835–1847,

doi:10.1063/1.859653.

[42] Thomsen, M. F., H. C. Barr, S. P. Gary, W. C. Feldman, & T. E. Cole (1983), Stability of Electron Distributions Within the Earth's Bow Shock, *J. Geophys. Res.*, *88*, 3035, doi:10.1029/JA088iA04p03035.

[43] Tsallis, C. (2023), *Introduction to Nonextensive Statistical Mechanics: Approaching a Complex World, 2nd edition*, Springer, ISBN:978-3-030-79569-6.

[44] Umeda, T., M. Ashour-Abdalla, D. Schriver, R. L. Richard, & F. V. Coroniti (2007), Particle-in-cell simulation of Maxwellian ring velocity distribution, *J. Geophys. Res.*, *112*, A04212, doi:10.1029/2006JA012124.

[45] Usami, S., & R. Horiuchi (2022), Pseudo-Maxwellian Velocity Distribution Formed by the Pickup-like Process in Magnetic Reconnection, *Frontiers in Astronomy and Space Sciences*, *9*, 846395, doi:10.3389/fspas.2022.846395.

[46] Vasyliunas, V. M. (1968), A survey of low-energy electrons in the evening sector of the magnetosphere with OGO 1 and OGO 3, *J. Geophys. Res.*, *73*, 2839–2884, doi:10.1029/JA073i009p02839.

[47] Vasyliunas, V. M., & G. L. Siscoe (1976), On the Flux and the Energy Spectrum of Interstellar Ions in the Solar System, *J. Geophys. Res.*, *81*, 1247–1252, doi:10.1029/JA081i007p01247.

[48] Wilson III, L. B., L.-J. Chen, S. Wang, S. J. Schwartz, D. L. Turner, M. L. Stevens, J. C. Kasper, A. Osmane, D. Caprioli, S. D. Bale, M. P. Pulupa, C. S. Salem, & K. A. Goodrich (2019), Electron Energy Partition across Interplanetary Shocks. I. Methodology and Data Product, *Astrophys. J. Suppl.*, *243*, 8 doi:10.3847/1538-4365/ab22bd.

[49] Wu, C. S., P. H. Yoon, & H. P. Freund (1989), A theory of electron cyclotron waves generated along auroral field lines observed by ground facilities, *Geophys. Res. Lett.*, *16*, 1461 doi:10.1029/GL016i012p01461.

[50] Xiao, F., R. M. Thorne, & D. Summers (1998), Instability of electromagnetic R-mode waves in a relativistic plasma, *Phys. Plasmas*, *7*, 2489–2497, doi:10.1063/1.872932.

[51] Xiao, F., Q. Zhou, Y. He, C. Yang, S. Liu, D. N. Baker, H. E. Spence, G. D. Reeves, H. O. Funsten, & J. B. Blake (2015), Penetration of magnetosonic waves into the plasmasphere observed by the Van Allen Probes, *Geophys. Res. Lett.*, *42*, 7287–7294, doi:10.1002/2015GL065745.

[52] Yoon, P. H., M. E. Mandt, & C. S. Wu (1989), Evolution of an unstable shell distribution of pickup cometary ions, *Geophys. Res. Lett.*, *16*, 1473–1476, doi:10.1029/GL016i012p01473.

[53] Yotsuji, T. (2010), *Random number generation of probability distributions for computer simulations*, Pleiades Publishing, Nagano [in Japanese].

[54] Zaheer, S., G. Murtaza, & H. A. Shah (2004), Some electrostatic modes based on non-Maxwellian distribution functions, *Phys. Plasmas*, *11*, 2246, doi:10.1063/1.1688330.

[55] Zank, G. P., J. Heerikhuisen, N. V. Pogorelov, R. Burrows, & D. McComas (2010), Microstructure Of The Heliospheric Termination Shock: Implications For Energetic Neutral Atom Observations, *Astrophys. J.*, *708*, 1092, doi:10.1088/0004-637X/708/2/1092.

[56] Zenitani, S., & S. Nakano (2022), Loading a relativistic Kappa distribution in particle simulations, *Phys. Plasmas*, *29*, 113904, doi:10.1063/5.0117628.

[57] Zenitani, S., & S. Nakano (2023), Loading loss-cone distributions in particle simulations, *J. Geophys. Res.*, *128*, e2023JA031983, doi:10.1029/2023JA031983.

[58] Zenitani, S. (2024a), A note on the flattop velocity distribution in space plasmas, *Research Notes of the AAS*, *8*, 30, doi:10.3847/2515-5172/ad225c.

[59] Zenitani, S. (2024b), A gamma variate generator with shape parameter less than unity, *Economics Bulletin*, *44*, 1113, arXiv:2411.01415.

[60] Zenitani, S. (2025), A simple procedure for generating a Kappa distribution in PIC simulation, *Research Notes of the AAS*, *9*, 299, doi:10.3847/2515-5172/ae1c41.

[61] Zenitani, S., S. Usami, & S. Matsukiyo (2026), Loading non-Maxwellian Velocity Distributions in Particle Simulations [Software], *Zenodo*, <https://zenodo.org/records/18225463>.

[62] Zirnstein, E. J., Möbius, E., Zhang, M., Bower, J., Elliott, H. A., McComas, D. J., Pogorelov, N. V., & Swaczyna, P. (2022), In Situ Observations of Interstellar Pickup Ions from 1 au to the Outer Heliosphere, *Space Sci. Rev.*, *218*, 28, doi:10.1007/s11214-022-00895-2.